CHALMERS

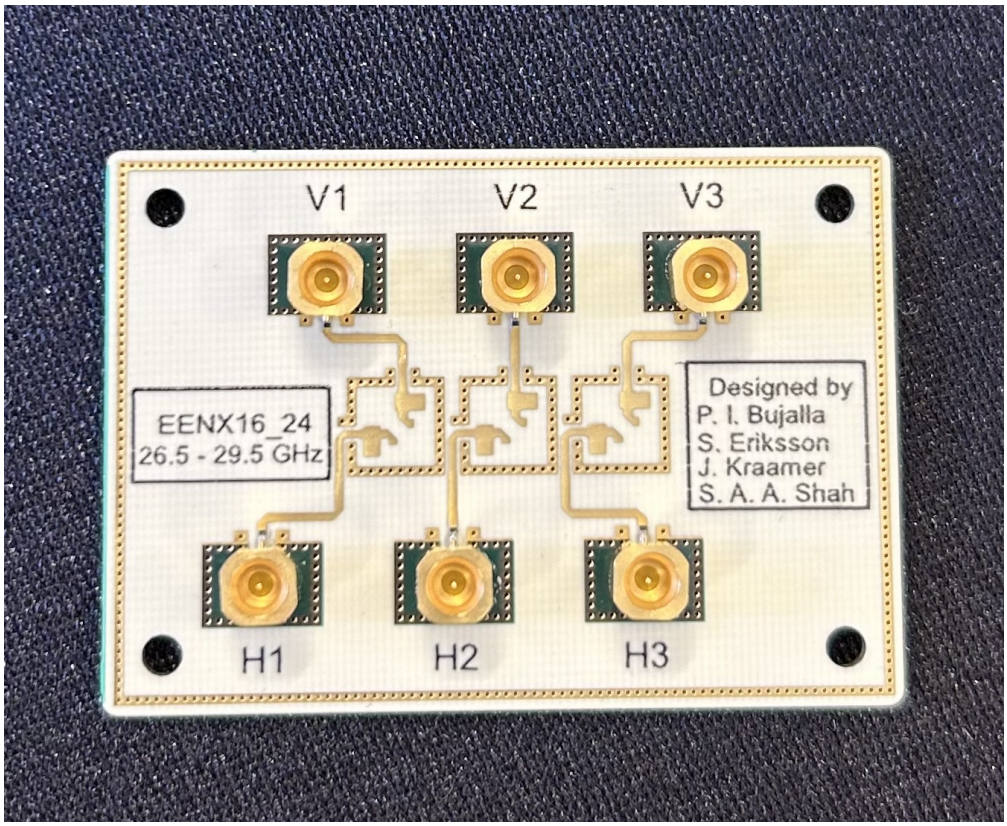

Designing a PCB microstrip antenna array for 5G mm-wave frequencies

Designing and testing a dual-polarized aperture-coupled microstrip patch antenna for the (26.5-29.5) GHz band

Bachelor's thesis in Electrical Engineering

Per Ingmar Bujalla, Simon Eriksson, Johanna Kraamer, Syed Ahsan Ali Shah.

DEPARTMENT OF ELECTRICAL ENGINEERING
CHALMERS UNIVERSITY OF TECHNOLOGY
Gothenburg, Sweden 2024
www.chalmers.se

Bachelor's thesis 2024

Designing a PCB microstrip antenna array for 5G mm-wave frequencies

Designing and testing a dual-polarized aperture-coupled microstrip patch antenna for the (26.5-29.5) GHz band

Per Ingmar Bujalla
Simon Eriksson
Johanna Kraamer
Syed Ahsan Ali Shah

CHALMERS

Department of Electrical Engineering
Division of Communications, Antennas, and Optical Networks
Chalmers University of Technology
Gothenburg, Sweden 2024

Designing a PCB microstrip antenna array for 5G mm-wave frequencies

Designing and testing a dual-polarized aperture-coupled microstrip patch antenna for the (26.5-29.5) GHz band

Per Ingmar Bujalla
Simon Eriksson
Johanna Kraamer
Syed Ahsan Ali Shah

Supervisor: Artem Vilenskiy, Department of Electrical Engineering
Examiner: Erik Ström, Department of Electrical Engineering

Bachelor's Thesis 2024
Department of Electrical Engineering
Division of Communications, Antennas, and Optical Networks
Chalmers University of Technology
SE-412 96 Gothenburg
Telephone +46 31 772 1000

Cover: The designed antenna array viewed from the matching network side.

Typeset in LaTeX
Printed by Chalmers Reproservice
Gothenburg, Sweden 2024

Designing a PCB microstrip antenna array for 5G mm-wave frequencies

Designing and testing a dual-polarized aperture-coupled microstrip patch antenna for the (26.5-29.5) GHz band

Per Ingmar Bujalla, Simon Eriksson, Johanna Kraamer, Syed Ahsan Ali Shah
Department of Electrical Engineering
Chalmers University of Technology

Abstract

This report presents the development and testing of a dual linearly polarized patch antenna array. The designed antenna covers the frequency range of (26.5-29.5) GHz, which also is known as the 5G NR FR2 n257 band. The antenna went through multiple iterations of simulation in Ansys HFSS, starting with the construction of a single element that then served as a building block for a three element array. After completing the array in HFSS it was sent for manufacturing. The project compares the simulated results to the ones from the tested manufactured array. For the antenna to be effective in a communication scenario, targets were set for various performance aspects including the radiation pattern, total efficiency and scattering parameters (S-parameters).

Each element in the array is aperture-coupled, cavity-backed and dual-polarized. The results showed that for a single isolated element, the peak broadside gain was 6.88 dBi for the vertical polarized port and 6.58 dBi for the horizontal polarized port. Moreover, the cross-polarization discrimination was > 14.6 dB, which suggest that it could be used for MIMO applications. It should be noted that these values are taken from the HFSS results as only the array and not the single element was manufactured.

The manufactured antenna underwent multiple tests. The S-parameters were measured with a VNA, the radiation pattern was measured in an anechoic chamber and lastly the total efficiency was characterized in a reverberation chamber. All measured and simulated S-parameters achieved the target. Beam steering capabilities were also investigated by phase shifting each elements in post-processing from the accumulated data of the radiation pattern. The test results from the manufactured array follow the simulated ones well in its S-parameters and radiation pattern. The measured total efficiency was above $> 75\%$. Finally, beam steering was achieved with a scanning range of $\pm 44^\circ$ for the simulated data and $\pm 46^\circ$ for the measured data.

Keywords: 5G, mm-wave, NR, antenna array, beam steering, aperture-coupled, dual-polarized, microstrip patch, cavity-backed, linear polarization, beam steering.

Acknowledgements

We would like to extend our sincere appreciation to those who have contributed to the completion of this project.

Firstly, we want to express our gratitude to our supervisor, Artem Vilenskiy, for his guidance and support throughout the project. His expertise and availability outside office hours have been pivotal in shaping the outcome of this work. You are awesome!

We are also grateful to our examiner, Erik Ström, for his insightful feedback and thoughtful suggestion, which have undoubtedly enhanced the report. Above all, we want to thank him for his continuous care in the project.

Furthermore, we would like to thank Ericsson for their involvement in this project. The opportunity to visit their company not only provided insights of the industry but also served as a source of motivation for finalizing this project.

Per Ingmar Bujalla, Simon Eriksson,
Johanna Kraamer och Syed Ahsan Ali Shah

Gothenburg, May 2024

List of Acronyms

Below is the list of acronyms that have been used throughout this thesis listed in alphabetical order:

AUT	Antenna Under Test
Cx	Cross (in cross polarized)
E	Electric
EEP	Embedded element pattern
EM	Electromagnetic
FR	Frequency range
MC	Mutual coupling
MIMO	Multiple-Input Multiple-Output
MISO	Multiple-Input Single-Output
MPA	Microstrip Patch Antenna
NR	New Radio
PCB	Printed Circuit Board
QoS	Quality of Service
SC	Smith chart
SGH	Standard gain horn
SIE	Single isolated element
SIMO	Single-Input Multiple-Output
SISO	Single-Input Single-Output
SMPM	Sub-Miniature Push-on Micro
TL	Transmission line
VNA	Vector Network Analyzer

Contents

List of Figures

List of Tables

1
Introduction

In recent years, there has been a significant increase in demand for wireless connectivity. What is, and can be, connected has become almost limitless, with devices ranging from personal computers to vehicles, machines and home appliances. The growing number of connected devices is expected to continue. Here the keyword is "5G", the backbone that enables all of this [1]. 5G is widely adopted and employed in many different application as a result of rapidly expanding wireless communications [2].

However, the adding of more devices pressures existing infrastructure [3]. Therefore, as the demand for internet reliability and greater capacity increases, so does also the demand in research for enabling higher data rates with better efficiency. This can be achieved by increasing the bandwidth (frequency range) [4].

Central to the 5G network is its ability to handle great capacity and the improved quality of services (QoS) in contrast to 4G systems [2]. Moreover, it can achieve a reaction time of less than 4 to 5 milliseconds (ms), offer speeds of up to 10 Gbps [5]. The 5G wireless communication uses a radio-access technology called New Radio (NR). The 5G NR is categorized in low-, medium- and high-frequency bands, where frequency range 2 (FR2) is part of the high-frequency bands. Further, the 5G NR FR2 n257 band refers to a frequency range of 26.5 - 29.5 GHz [6, p. 27-36].

Since antennas transceive the signals, they are a crucial component for communication systems and its design should therefore be considered when finding cost-effective solutions for increasing the 5G network availability. The microstrip antenna is a top candidate given that it is cheap to manufacture and has a low-profile design, whilst still having versatility in changing the radiation pattern and polarization. Since Printed Circuit Board (PCB) technology has good scalability [7], arrays of them can easily be made which further enhances its capabilities by enabling a greater directivity and beam steering functionality [8, p. 783-785, p.832-837].

1.1 Purpose

The purpose of the study is to design, manufacture and test a 5G mm-wave low-profile antenna operating in the 5G NR FR2 n257 band. It is intended to be compact and efficient with good radiation characteristics, to ensure broad coverage and high capacity in densely populated areas where numerous devices are interconnected. The antenna array will comprise of several identical elements, each with dual-polarization capabilities. This

setup allows for better signal reception and transmission, accommodating the increasing number of connected devices in modern communication networks.

The study will involve comparing simulated performance with real-world testing results to evaluate the effectiveness of the antenna. In addition, the purpose is to explore the ability to steer the signal in specific directions, potentially improving signal strength and quality in targeted areas.

1.2 Scope

The design and test phase of the study is a subject to limitations. The study is focused on the PCB patch resonator antenna, due to its low-profile design aligning with the purpose of the study, and its widespread use in existing 5G network systems. Moreover, the geometric shape of the patch antenna this study aims to analyze is exclusively rectangular. Other symmetrical shapes such as circular, also applicable in dual-polarized antenna arrays, but they are disregarded in this report. Exclusively focusing on one shape of antenna, the study aims to optimize the performance of this type of design.

It was decided to focus on one type of feeding method, the aperture-coupled feeding method, which is the most common type of feeding for dual-polarized antenna arrays and offers design flexibility [9]. Other feeding methods such as probe feed, microstrip-line feed and proximity-coupled feed will not be included. The reason for not including probe feed and microstrip-line feed is due to cross-polarized radiation [8, p. 786], where the vertical polarized field influences the horizontal polarized field and vice versa. The research around the proximity-coupled feeding method implemented for antennas with dual-polarization is limited [10], therefore the method is discarded in this project.

The manufacturing of the PCB will also add some restrictions for the dimensions and choice of dielectric material. Other design requirements are that the area of a single antenna element should be less than 6x6 mm^2 and the total thickness of the PCB should be less than 1.5 mm. A Sub-Miniature Push-on Micro (SMPM) connector will be used for its small dimension, making it easier to fit on the PCB.

Furthermore, when simulating and testing the radiation characteristics of the antenna, it will only consider the far-field. The reason for excluding the near-field effects is because of its modeling complexity and irrelevance for the communication scenarios of this project.

1.3 Research Questions

The project will aim to answer the following questions:

- How can a microstrip patch antenna (MPA) array be designed with given design constraints?
- How do the results from simulations of the antenna array in Ansys HFSS compare to the results of the manufactured antenna?
- Is it possible to implement beam steering capabilities on the designed antenna array?

1.4 Social and Ethical Aspects

The antenna studied and developed in this report is by itself only a passive component meaning it is useless without an active system behind it. Instead, the ethical aspects of the broad infrastructure behind it, including the whole communication system, should be considered.

The development and expansion of internet infrastructure entails both benefits and drawbacks. It will interconnect more people and devices, enabling almost instant communication. This can lead to increased efficiency in both individual and industrial work, bolster safety through monitoring devices, and foster innovation in new services and products.

As for the negative aspects, excessive reliance on stable internet connections can heighten society's vulnerability to situations such as hacker attacks and electrical blackouts. The internet infrastructure itself also consumes a lot of power, given that it always has to be on to provide its services. If the antennas are not powered from renewable energy sources, it could result in a negative impact on the environment. Lastly there is also the impact on the individual level in the form of radiation exposure. However, the current levels of exposure are significantly lower than the recommended reference level from the Swedish Radiation Safety Authority [11]. On the other hand, the effects of radiation exposure on animals are not fully assessed.

One ethical aspect of the antenna manufacturing is the use of resources. Prevalent conductors used for MPAs and PCBs are gold and copper [8]. These metals are in high demand and excavation of these minerals have a significant impact on the environment [12]. The metal ore mining industry produces a significant amount of slag, dust and aerosols, which can contain toxic materials such as As, Cd, Hg and Pb. These heavy metals contaminate both terrestrial and aquatic environments. The refining process of the ores produces large volumes of SO_2 causing acidification of the rain which can be harmful of trees, crops and structures in contact of the rain.

2

Theory

The following chapter delves into the theory and technical terms used in the project. It will start with an overview of the fundamental function of an antenna and the figures of merit. Thereafter, it will move on to polarization of electromagnetic (EM) waves, grouping of antenna elements and then transmission line (TL) theory. Lastly, the chapter will present the theory behind the specific antenna design used in the project.

2.1 Fundamentals of Antenna Theory

An antenna transfers EM waves between guided and radiating waves in free space and vice versa [13], [14, p. 600], [8, p. 1-24]. To create radiation, there must be a time-varying current or acceleration of charges within the conducting materials [8, p. 1], [14, p. 600], [15]. The following equation provides basic relation between current and charge and also serves as the fundamental relation of EM radiation for a z-directed single wire

$$l\frac{dI_z}{dt} = lq_l a_z, \tag{2.1}$$

where l is the length of the wire, q_l is the charge per unit length, I_z is the current through the wire and a_z is the acceleration of charges. The subscript indicates the z-direction in right hand coordinate system.

Creating charge acceleration on a wire is dependent on the geometrical structure and EM properties of the material[8, p.1-24]. Therefore various type of antennas have been developed/designed with different shapes to achieve various radiation patterns [15], [8, p.1-24]. Common examples includes different wire shapes such as dipoles, long wires and helices. Additionally, there exists aperture types such as open-ended waveguides, slots and horns, which use guiding waves discontinuities for creating radiation.

A passive antenna can function as either a transmitting or receiving antenna [16, p. 249–293]. In both roles, its radiation properties and impedance remain the same, a principle known as reciprocity. Essentially, if an antenna emits maximum power in a specific direction during transmission, it will also be the most sensitive to receiving waves coming from that same direction.

2.2 Antenna Parameters and Figures of Merits

Understanding how antennas perform involves an exploration of various factors that influence their functionality [8, p. 26-88], [16, pp. 249–293,], [17], [14, p. 607]. These factors includes key radiation characteristics such as field pattern, directivity, gain, impedance, efficiency and bandwidth.

2.2.1 Radiation Pattern

The radiation pattern of an antenna describe how it emits EM waves in different directions [18, ch. 1.4], [8, p. 25-39]. It is commonly depicted using spherical coordinates, denoted as the electric field vector $\mathbf{E}(R, \theta, \phi)$ and magnetic field vector $\mathbf{H}(R, \theta, \phi)$, with the antenna located at the origin. Here θ represent the elevation angle, ϕ the azimuth angle and R radial distance from the origin as illustrated in the accompanying figure 2.1.

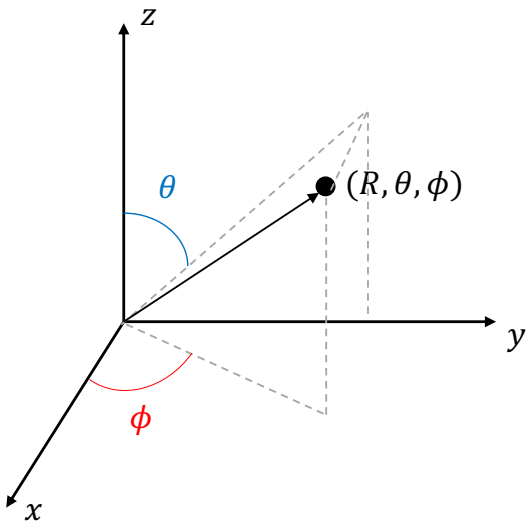

Figure 2.1: Spherical coordinate system where (R, θ, ϕ) denotes the field point.

This pattern is primarily studied in the far field, which typically begins at a distance, R, from the antenna element, where R satisfies the condition

$$R > \frac{2D^2}{\lambda_0}, \tag{2.2}$$

where D denotes the largest dimension of the antenna and λ_0 is the wave length in free space at resonance frequency.

The field intensities can then be used to calculate the radiated power in far field [19]

$$P_{av} = \frac{1}{2}\Re\{\mathbf{E} \times \mathbf{H}^*\}, \tag{2.3}$$

$$P_{\text{rad}} = \int_{\theta=0}^{\pi} \int_{\phi=0}^{2\pi} P_{\text{av}} \cdot R^2 \sin\theta \, d\theta \, d\phi. \tag{2.4}$$

This integral represents the total radiated power over all solid angles, calculated as the product of the average power density P_{av} and the surface area of a sphere at radius R.

2.2.2 Directivity and Gain

Directivity, D, and gain, G, are fundamental parameters that assess how the power density emitted by an antenna compares to that of a standard reference antenna [18]. This reference antenna is typically assumed to be an ideal isotropic radiator, distributing all input power evenly into radiated power. While the radiation pattern, and thus directivity and gain, typically vary based on the angles θ and ϕ, attention is often focused on the maximum values within the main beam.

The directivity, or directive gain, D of an antenna pattern is defined as the ratio of the radiation intensity $U(\theta, \phi)$ in the direction (θ, ϕ) to the average radiation intensity in all directions [8, p. 41]. The total average radiation intensity is equal to 4π multiplied with the total radiated power P_{rad}. If a specific direction is not specified, the directivity refers to the direction of maximum radiation intensity U_{max}. Some sources, such as [14], distinguish these as two different parameters, where directivity only refers to the ratio with the maximum radiation intensity U_{max}, whilst for a specific direction (θ, ϕ), the ratio is denoted directive gain G_D. This report will equate directivity with directive gain, which is written as

$$D\left(\theta, \phi\right) = \frac{4\pi U\left(\theta, \phi\right)}{P_{\text{rad}}}. \tag{2.5}$$

Directivity is commonly measured in decibels relative to an isotropic radiator (dBi). The radiating intensity $U(\theta, \phi)$ is a measure of the power density radiated by the antenna in a specific direction (θ, ϕ) per unit solid angle and is derived from the following equation [8, p. 38]

$$U\left(\theta, \phi\right) = R^2 P_{av} = \frac{R^2}{2\eta}|\mathbf{E}(R, \theta, \phi)|^2, \tag{2.6}$$

where η is the intrinsic impedance of the medium and $\mathbf{E}$ is the far-zone electric field intensity. The intrinsic impedance in free space η_0 is equal to 120π [14, p. 374].

Another figure of merit is the power gain, often simply referred to as gain, which indicates the efficiency of the antenna [14, p. 611]. This is the ratio of radiation intensity to input power accepted by the antenna port P_{in}, given by [8, p 62]

$$G(\theta, \phi) = \frac{4\pi U(\theta, \phi)}{P_{\text{in}}}, \tag{2.7}$$

where $P_{\text{in}} = P_{\text{rad}} + P_{\text{loss}}$, with P_{loss} representing power loss due to heat radiation and other nearby structures [14, p. 612].

Impedance mismatch in the connected circuitry of the antenna can reduce its gain as the actual received power may fall short of the theoretical value due to impedance mismatch in transmission line supplying the antenna [8, p. 60-63], [13]. To count for this, the realized gain $G_{re}(\theta, \phi) = \alpha G(\theta, \phi)$ is considered, where α is the impedance mismatch factor. This can also be expressed using the passive input reflection coefficient $|\Gamma|$ as $\alpha = (1 - |\Gamma|^2)$.

The radiation efficiency of the antenna η_r, measures how effectively it converts accepted power into radiating power in the far field region [14, p. 612]. It is calculated as the ratio of gain to directivity

$$\eta_r = \frac{G}{D} = \frac{P_{\text{rad}}}{P_{\text{in}}}. \tag{2.8}$$

It is important to note that these parameters are expressed for a single-port antenna. For the total efficiency, the accepted power P_{in} is replaced by the supplied power to the antenna in the equation above [20].

2.2.3 Scattering Parameters

Scattering parameters (S-parameters) are used to explain how the EM-waves behave in an electrical circuit. Each S-parameter is connected to a specific measurement and is represented by a complex number with a magnitude ranging between 0 and 1. When evaluating how well a circuit is impedance matched (this is explained in Section 2.5.2), a magnitude of 0 is an ideal matched circuit as no reflection takes place. The opposite is when the magnitude is 1, meaning that a total reflection takes place. S-parameters are defined according to the following equation [21, p 178]

$$S_{ij} = \left.\frac{V_i^-}{V_j^+}\right|_{V_k^+=0 \text{ for } k \neq j}, \tag{2.9}$$

where j refers to the port where the voltage is driven and i is the measured port. V_i^- is the voltage of the reflected wave from port i and V_j^+ is the voltage of the incident wave on port j.

For a system with two ports, a matrix can be used for representing the S-parameters as depicted below

$$S = \begin{bmatrix} S_{11} & S_{12} \\ S_{21} & S_{22} \end{bmatrix}. \tag{2.10}$$

S_{11} and S_{22} represents the input and output port reflection, these are the ratio between the incident reflected wave and the emitted wave from the port. Furthermore, S_{12} and S_{21} represent the reverse gain and forward gain. The ratio of the transmitted signal from port 2 reaching port 1 and vice versa.

The size of the S-parameter matrix is decided by the amount of ports in the system. A system with n ports produces a matrix of the size n x n.

2.3 Polarization

The polarization explains how the EM waves propagates in free space, as a function of time, when radiated from the antenna [8, p 66]. The different types of polarizations of antennas are linear, circular and elliptical, determined by the shape of the antenna element and how the antenna is excited.

The EM waves radiating from a linear antenna are aligned with one plane, often referred to as a vertical or a horizontal plane, which is orthogonal to the direction of propagation [22]. A linearly polarized antenna can only transceive signals oriented in the same plane as the polarization. Losses in power can occur due to polarization mismatch [8, p 71]. The polarization of antennas are relatively consistent through the main lobe, but can vary in the minor lobes of the antenna [22].

Dual-polarized antennas uses both vertical and horizontal polarization simultaneously [23]. Having two polarizations allows the antenna to transceive information in two channels. These channels can in theory be completely independent from each other if the two EM waves emitted in the channels are fully orthogonal to each other. In practice however, the two channels are seldom fully orthogonal and can affect each other. The phenomenon is referred to as cross-polarization. Thus, to allow for a clearer signal, a high cross-polarization discrimination is of interest when designing an dual-polarized antenna.

The cross-polarized (Cx) component is the part of the electric (E) field that is orthogonal to the co-polarized component in the propagation plane [24]. The co-polarized component is the part of the E-field that follows the same polarization direction as the dominant field in the aperture plane. The aperture plane is the projection of the propagation plane on the xy-plane.

Dual-polarization can be implemented on various shapes of antennas. To implement dual-polarization the antenna has to be fed from two orthogonal directions, creating two orthogonal E-fields [23]. Having multiple feeding points to the same antenna element can lead to polarization channels mutual coupling (MC). This is the influence that the ports have on each other and is described by the S-parameters, S_{12} and S_{21}, as mentioned in Section 2.2.3.

2.4 Antenna Array

Multiple antenna elements operating together creates an antenna array. Usually the antenna elements are identical [8, p. 285]. PCB antennas operating at high frequencies are commonly put in array arrangements to achieve a higher gain [21, p. 578]. Placing antennas in an array formations brings complications, such as array element MC [25]. Array element MC implies that EM fields of the elements in an array configuration interacts and influences other elements in the array. This interaction leads to energy losses, since the energy excited from one port is received back into another. Various methods can be utilized to address element coupling in the design process. [26, ch. 1.9]. One method to

measurements of magnitude of array element MC is described by S-parameters [25].

For a linear array consisting of identical array elements, the following equation can be used to describe the radiation pattern of the array [8, p. 293-294], [16, p. 280]

$$E_{total} = E_1 \cdot AF, \tag{2.11}$$

where E_{total} is the far-zone field of the array, and E_1 is the far-zone field of one single element of the antenna. AF is defined as the array factor and is derived from the geometry of the antenna and the operating frequency as [8, p. 293-294]

$$AF = \sum_{n=1}^{N} e^{j(n-1)\Psi}, \tag{2.12}$$

$$\Psi = kd\cos(\theta) + \beta, \tag{2.13}$$

where $k = \frac{2\pi}{\lambda_0}$ is the wave number, d is the spacing between the elements, θ is the observation angle, β is an external phase shift and N is the number of elements.
An important assumption for the array factor equation is that all of the elements are identical, meaning that E_1 is the same for every element and that they are equally spaced with a distance d.

2.4.1 MIMO

Multiple-Input Multiple-Output (MIMO) is a system technology that uses multiple antennas for transmitting and receiving radio waves. This technology aims to increase data rates by allowing multiple channels between transmitter and receiver in parallel, known as spatial multiplexing [16].

Today MIMO technology is used in applications for wireless communication such as wifi-networks and cellular devices. Massive MIMO antennas are deployed to support the high demanded data rates of 5G NR in densely populated areas [27].

Systems using MIMO technology require extensive computational power in comparison to other systems utilizing technologies such as, Single-Input Single-Output (SISO), Single-Input Multiple-Output (SIMO) and Multiple-Input Single-Output (MISO) [28]. This increased complexity thus results in more expensive hardware requirements for antenna systems utilizing MIMO technology.

2.4.2 Beam Steering

The concept of beam steering is to not physically move the antenna structure yet change the direction of the antennas main lobe [16, p. 290-292], [8, p. 287]. One way of doing it, is by changing the phase of the elements that are excited. This procedure will be described in more detail below. The total E-field of an arbitrary antenna array is same as Equation (2.11).

This indicates that E_{total} is the greatest when AF from Equation (2.12) is equal to N, as this would result in a summation of all elements E_1 -fields when they are in phase [8, p. 302]. This happens when $\Psi = 0$ and is achieved by choosing β accordingly to cancel out the phase difference $kd\cos(\theta)$ in Ψ. The main lobe can then be directed to a desired angle θ.

Given this, when the elements in the array are not exactly the same, but their E-fields are known (magnitude and argument) then the phase shift β will be the conjugate of the E-fields argument for the desired scan angle θ, as this will make $\Psi = 0$ for each element. E_{total} is then, just like for the case with identical elements, the summation of each E-field.

2.4.2.1 Grating Lobes

There are cases when beam steering gets restricted by grating lobes. These are additional lobes apart form the main lobe that can appear for certain steering angles [29, p. 44]. The position of the steering angle θ_0 in relation to the angle of an arbitrary grating lobe can be derived from

$$\sin\theta_p = \sin\theta_0 + \frac{p\lambda}{d}, \quad p \in Z, \tag{2.14}$$

where p constitutes the number of grating lobe relative to the main lobe (e.g. $p = 1$ is the next lobe to the right in the θ-plane), θ_p is the position of the grating lobe, θ_0 is the position of the main lobe and d is the distance between the antenna elements. The grating lobe is only relevant when it appears in the positive z-plane, hence when $\theta_p = -90° \rightarrow 90°$ which corresponds to the 180° scanning range of the array. As a result, the maximum beam steering angle $\theta_{\mathrm{m},0}$ can be found when the closest grating lobe $p = -1$ appears at $\theta_p = -\frac{\pi}{2}$. Using this premise, Equation (2.14) becomes

$$\sin\theta_{\mathrm{m},0} = -1 - \left(\frac{-\lambda}{d}\right) = \frac{\lambda}{d} - 1 \implies \tag{2.15}$$

$$\theta_{\mathrm{m},0} = \arcsin\left(\frac{\lambda}{d} - 1\right). \tag{2.16}$$

From the same equation it can be derived that the maximum distance d between elements, to stay free from grating lobes when scanning is $\frac{\lambda}{2}$.

2.5 Transmission Line

Transmission lines (TL) allows for a controlled propagation of EM energy and it consist of two or more wires [21, p. 47]. The model for it is a resistor and an inductor in series with a capacitor and conductance in parallel. The equation below is from [21, p. 48] and describes the state of the wave at any given point.

$$V(z) = V_0^+ e^{-\gamma z} + V_0^- e^{\gamma z}, \tag{2.17}$$

$$I(z) = I_0^+ e^{-\gamma z} + I_0^- e^{\gamma z}, \tag{2.18}$$

here V_0 refer to the voltage at the start of the TL and the propagation constant γ is calculated according to

$$\gamma = \alpha + j\beta = \sqrt{(R + j\omega L)(G + j\omega C)}. \tag{2.19}$$

Here R is the resistance, L the inductance, G the conductance and C the capacitance. A TL has a characteristic impedance which is what the EM wave sees for every length $\Delta z \to 0$ of the line [21, p. 49]. The following equation for the impedance can be derived from (2.17), (2.18), (2.19).

$$Z_0 = \frac{V_0^+}{I_0^+} = \sqrt{\frac{R + j\omega L}{G + j\omega C}}. \tag{2.20}$$

The convention is that the real part of characteristic impedance is set to either 50 or 75 Ω. If maximum power transfer is desired it is crucial that the same impedance is held from from generator to the load. Otherwise, the load has to be impedance matched to the characteristic impedance of the TL. The impedance match or mismatch can be shown by the following equation for the reflection coefficient Γ [21, p. 55]

$$\Gamma = \frac{V_0^-}{V_0^+} = \frac{Z_L - Z_0}{Z_L + Z_0}. \tag{2.21}$$

If the load $Z_L = Z_0$, then Γ is 0, indicating that there are no reflected waves on the TL. As a result, all the power is absorbed by the load.

To visualize this, the return loss coefficient can be plotted logarithmically (dB) [21, p. 55]

$$RL = -20 \log |\Gamma|. \tag{2.22}$$

Another tool for analyzing TL is the Smith Chart (SC). It plots the normalized impedance for frequencies in the complex Γ plane. A matched impedance lies in the center of the chart [21, p. 60].

2.5.1 Microstrip

The type of TL used in this project is a microstrip [21, p. 136]. It is a metal strip that sits over a ground plane separated by a dielectric substrate. The characteristic impedance of the microstrip can be chosen by changing the height over the ground plane, the width of the strip or the permittivity of the substrate. The following equation from [21, p. 138] calculates the width W of the microstrip with the condition that $\frac{W}{d} < 2$, where d is the height of the substrate:

$$W = d\frac{8e^A}{e^{2A} - 2}, \tag{2.23}$$

where

$$A = \frac{Z_0}{60}\sqrt{\frac{\epsilon_r + 1}{2}} + \frac{\epsilon_r - 1}{\epsilon_r + 1}\left(0.23 + \frac{0.11}{\epsilon_r}\right), \tag{2.24}$$

and ϵ_r the permittivity of the substrate.

2.5.2 Impedance Matching

As previously mentioned, when the load connected to the TL is mismatched, one has to impedance match for maximal power transfer [21, ch. 2]. It can be done by adding reactive components in series or parallel, adding or subtracting TL length, changing its resistance or a combination of all. Here the SC is a useful tool to calculate the reactance needed for impedance matching. The SC for an arbitrary TL (blue circle) is displayed in Figure 2.2. Then from the impedance, the matching components can be determined. At microwave frequencies it is convenient to use stubs and TL lengths to match the circuit as these eliminate the need for external components.

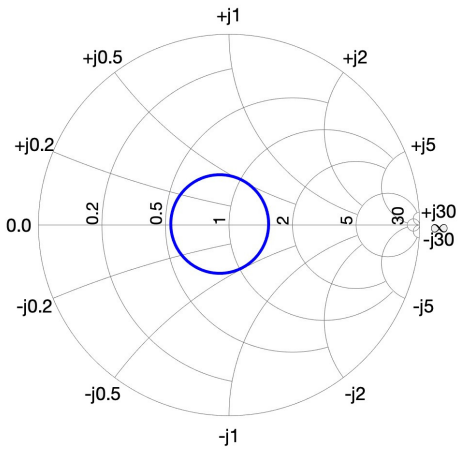

Figure 2.2: Smith chart displaying an arbitrary transmission line.

2.6 Microstrip Patch Antennas

A microstrip patch antenna (MPA) is essentially a structure where a radiating element, typically a patch, is placed on the top of a dielectric substrate, while the ground plane is located on the underside of the substrate [30]. The patch is made from conductive materials like copper and gold [8, p. 785]. Typically, the patch is printed onto a microwave substrate material with a relative permittivity, ϵ_r, falling within the range of 2 to 10. However, the choice of the material can vary depending on the specific requirements of the application [30],[31].

MPA technology has multiple strengths both operational and practical, including highly adaptable frequency ranges, flexibility in feed line design and the ability to achieve beam

scanning for antennas in array formation [30]. Operational disadvantages with the technology are low power and narrow frequency bandwidth, but these characteristics are in some cases wanted [8, p 783]. Further disadvantages of MPAs are linked to the low efficiency, low polarization purity and the presence of spurious feed radiation.

Due to the ease of analysis and fabrication, rectangular and circular patches are the most commonly used shapes. Various other shapes such as ellipses, annular rings and triangles can also be employed as long as they exhibits a well defined resonant mode [30], [8, p. 785]. Apart from the patch shape and choice of substrate, MPAs also differs in terms of feeding techniques.

2.6.1 Fringing Effects and Patch Size

Patch antennas are influenced by a phenomenon known as fringing effects [8, p 788]. Fringing effects occur due to the finite length of the patch, leading to the E-fields at the edge curling back into the substrate, visualized in Figure 2.3. As a result, the electrical length of the patch increases, meaning that the patch appears longer than it physically is.

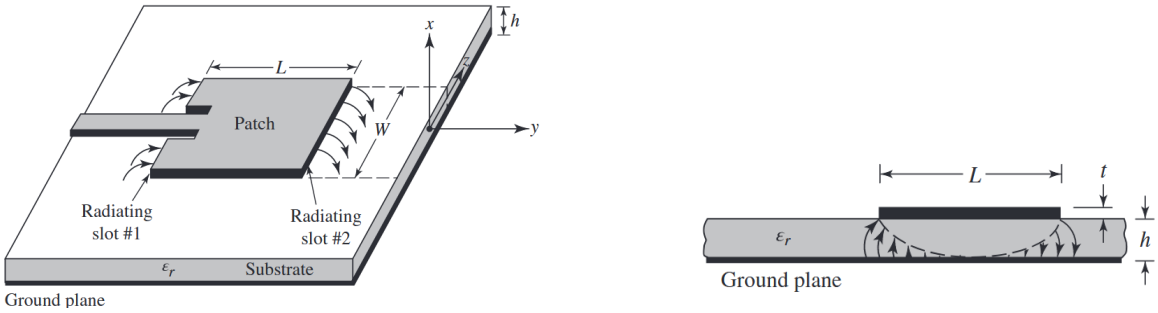

(a) Microstrip Antenna. **(b)** Side view.

Figure 2.3: MPA with fringing effects, images taken from [8, p 784] reproduced with permission.

The fringing effect is dependent on the relation between the substrate height and the size of the patch antenna.

The TL model is the easiest model to use when designing a rectangular MPA, but has the lowest accuracy [8, p 788]. The design procedure of a rectangular patch following the TL model starts with specifying the dielectric constant ϵ_r, substrate height h and the resonance frequency f_r. The width of the radiating element is then given by

$$W = \frac{c_0}{2f_r}\sqrt{\frac{2}{\epsilon_r + 1}}, \tag{2.25}$$

where c_0 is the speed of light in space. If the relation between patch width and substrate height follows $W/h > 1$, the width can be used to determine the effective dielectric

constant $\epsilon_{r,\text{eff}}$ as

$$\epsilon_{r,\text{eff}} = \frac{\epsilon_r + 1}{2} + \frac{\epsilon_r - 1}{2}\left[1 + 12\frac{h}{W}\right]^{-1/2}. \tag{2.26}$$

The increase of electrical length ΔL due to fringing effects is acquired by inserting the width and effective dielectric constant into the following equation

$$\frac{\Delta L}{h} = 0.412\frac{(\epsilon_{r,\text{eff}} + 0.3)\left(\frac{W}{h} + 0.264\right)}{(\epsilon_{r,\text{eff}} - 0.258)\left(\frac{W}{h} + 0.8\right)}. \tag{2.27}$$

To obtain the physical length L of the patch the following equation is used

$$L = \frac{c_0}{2f_r\sqrt{\epsilon_{r,\text{eff}}}} - 2\Delta L. \tag{2.28}$$

Usually the length of rectangular MPAs vary between

$$L = a\frac{\lambda_0}{\sqrt{\epsilon_r}} = a\lambda_d, \quad 0.47 \leq a \leq 0.49, \tag{2.29}$$

where λ_0 and λ_d is the wavelength of the resonance frequency in space and in the dielectric respectively [8, p 791].

2.6.2 Substrate

The antenna elements are printed on usually very thin dielectric films [32, p. 1-33]. These films have two crucial parameter which can affect the antenna performance: the height and the permittivity. Different heights of substrates influence the frequency, gain and return loss [33]. The substrate height influences the bandwidth and resonance frequency of the antenna. An increase in substrate height decreases the resonance frequency and increases the bandwidth [34]. A higher ϵ_r results in a more narrow bandwidth compared to a lower value [8, p 785].

2.6.3 Feeding Techniques

There are multiple ways to excite a MPA. Different feeding methods are used based on the application and limitations of the antenna. The most commonly used feeding methods are microstrip line, probe, aperture-coupling and proximity-coupling [8, p 785]. In Figure 2.4 the different feeding methods are shown.

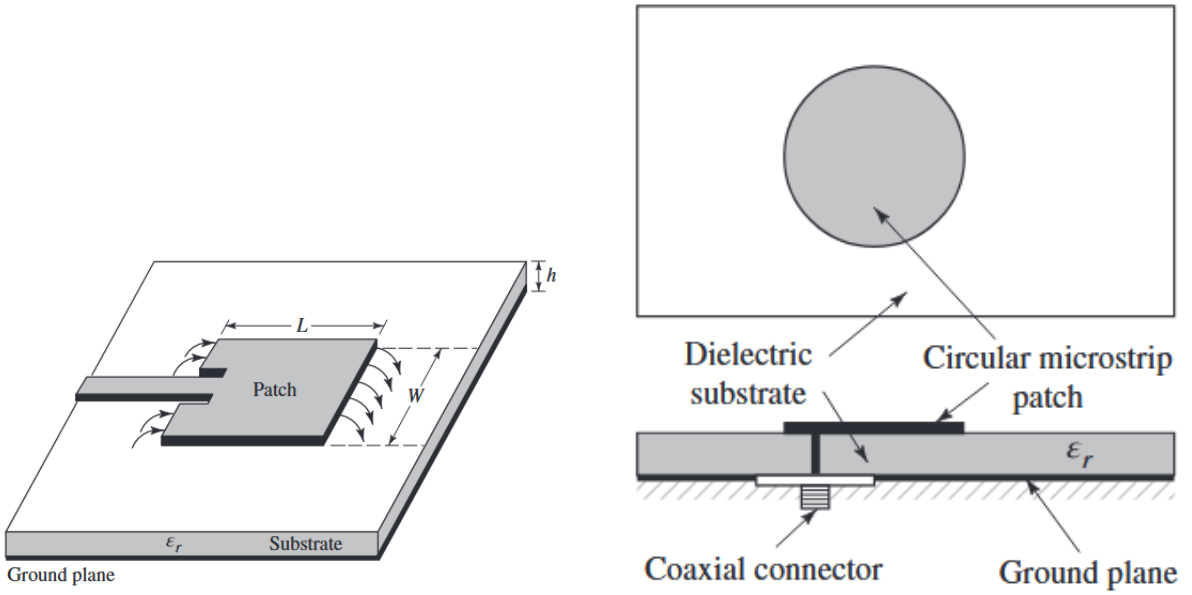

(a) Microstrip line feed.

(b) Probe feed.

(c) Aperture-coupled feed.

(d) Proximity-coupled feed.

Figure 2.4: The four most commonly used feeding methods for MPAs, images taken from [8, p 786] reproduced with permission.

The different feeding methods have different strengths and weaknesses. The advantage of the microstrip line feed MPA is its easy fabrication process and matching. However, it has comparably stronger surface waves and spurious feed line radiation field, which influences the performance of the antenna [8, p 785]. Similar to the microstrip line feed MPA, the probe feed is also easy to fabricate and match and has lower spurious radiation from the feeding probe. The drawbacks of using a probe feeding method is that the antenna is more difficult to model with substrates height $> 0.02\lambda_0$. Both microstrip line and probe feed have a higher cross-polarization radiation due to asymmetries in the structure, this being more apparent in high frequency applications.

Aperture-coupled feed has its strengths in its low spurious radiation and the low influence from the feed line on the patch radiation, due to the ground plane separating the feed strip and the radiating element. Consequently, the polarization purity is increased [8, p 787]. It also is rather easy to model due to having two separate substrates, allowing substrates to be selected in order to optimize the performance for both the feed line and the radiating element. The drawbacks of using aperture-coupling is that it is the most

difficult to fabricate.

Proximity-coupled feed has the best bandwidth out of the four feeding methods, and like aperture-coupled feed it is rather easy to model and is hard to fabricate [8, p. 787].

Aperture-coupled MPAs consists of two, or more, layers with dielectric materials. The feed line is situated on one layer while the radiating patch is positioned on another [35]. The two layers are separated by a ground plane with a cut out slot, as depicted Figure 2.4c. The ground plane isolates the antenna element from unwanted radiation from the feed line, resulting in increased polarization purity. Aperture-coupled MPAs are excited through a slot [8, p 841]. The shape, size and positioning of the slot affects the characteristics of the antenna and its resonance frequency. Tuning these parameters are essential when designing MPAs.

2.6.4 Cavity-backed Antenna

A cavity-backed MPA is characterized by enclosing a volume underneath the radiating element, often done with vias, forming a backing cavity as seen in Figure 2.5 [36]. The dimension of the cavity is chosen assuming that one of the lowest mode is excited within it [37]. A mode is a description of the field pattern for a propagating EM wave. The transverse electric TE_{101} mode is typically selected as the lowest mode for the rectangular backing cavity. For the TE mode the E-field in the direction of propagation, E_z, is zero, whilst the magnetic field H_z is non-zero [14, p. 524]. This mode is significant because it represent the fundamental mode for the cavity geometry, influences the antenna performance and radiation characteristics [38].

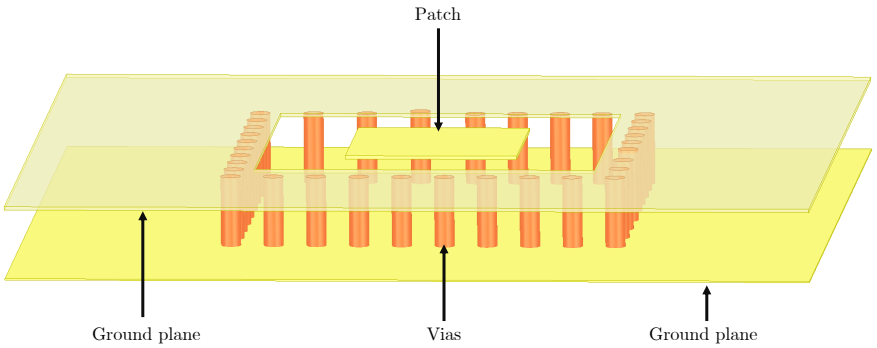

Figure 2.5: A volume enclosed by vias forming a cavity-backed patch antenna.

Cavity-backed MPAs aim to reduce the influence of surface waves that occur within the dielectric material of the antenna [8, p 181]. Surface waves are amplified when the height of dielectric material in the substrate is increased [8, p 783]. Surface waves are not wanted

since they extract a portion of the total energy that could be used for radiation, leading to reduced gain when substrate height increase. Another drawback of surface waves is that they influence the antennas radiation pattern and polarization characteristics. In antenna arrays surface waves can lead to antenna element MC which is undesirable. Furthermore surface waves in antenna arrays can affect the scanning capabilities leading to so called array scan blindness, meaning there are nulls in the radiation pattern of the array caused by large variations of the reflection coefficient [8, p 478].

3
Methods

The method consists of three primary parts: design and simulation, manufacturing and tests.

3.1 Design and Simulation

The process of designing the MPA was divided into four sub-designs. Initiating with a single-polarized single element antenna model, progressing to a dual-polarized single element antenna model, followed by connector integration and concluding with development of the final complete three element linear antenna array.

The 3D model of the MPA was designed using the software Ansys HFSS. It is a simulation software for EM models, mainly high frequency electronics, such as antennas and microwave components [39]. The development process utilized simulation driven EM analysis to describe the characteristics of the antenna design. Multiple simulations for each sub-design where conducted and compared in order to optimize the different parameters of the antenna model.

3.1.1 Manufacturer Limitations and Performance Targets

In order to ensure effective implementation of the antenna into a 5G network the antenna should meet a number of performance requirements, which are presented in the following list.

- Frequency range between 26.5-29.5 GHz.
- Two linear polarizations, one horizontal and one vertical.
- Peak broadside gain of > 5 dBi.
- Coverage of $\pm 60°$ range where the radiation pattern non-uniformity is < 6 dB.
- Cross-polarized discrimination efficiency of > 10 dB.
- Total efficiency of > 70 %.

Additionally, Table 3.1 presents the requirements for the S-parameters of the antenna. Because it is a three element array where each element is dual polarized, it will create a 6x6 S-parameter matrix. Table 3.2 depicts which port relates to which subscript for the S-parameter. H stands for the horizontal polarization and V for the vertical polarization.

Table 3.1: The antenna target performance for the scattering parameters.

Parameter	**Quantity**	**Target**
Input reflection coefficients	S_{11}, S_{22}, S_{33}, S_{44}, S_{55}, S_{66}	< -10 dB
Polarization self-coupling (intra-cell) coefficients	S_{12}, S_{34}, S_{56}	< -15 dB
Cross-polarized element mutual coupling (inter-cell) coefficients	S_{14}, S_{16}, S_{23}, S_{25}, S_{36}, S_{45}	< -18 dB
Co-polarized element mutual coupling (inter-cell) coefficients	S_{13}, S_{15}, S_{24}, S_{26}, S_{35}, S_{46}	< -18 dB

Table 3.2: Description of which port relates to which subscript for the S-parameter.

Subscript (i, j)	Port
1	H1
2	V1
3	H2
4	V2
5	H3
6	V3

The manufacturer has limitations for manufacturing the PCB, which has to be considered when designing the antenna. The limitations given by the manufacturer, Eurocircuits, are listed on their website [40]. These involve lower limitations in trace size, via size and distances between parts.

The limitation of a total PCB thickness of less than 1.5 mm was taken into account when choosing from materials. Material as well as thickness of substrates was determined by availability from the manufacturer, which was found in the data sheets. The coorperation Rogers have different series of laminates and prepegs [41], where the RO4000 series is used for applications in mm-wave frequencies. The laminate RO4350 was chosen for the substrate below the patch and above the feed. The height for the patch substrate was selected to 0.76 mm and the substrate height for the feed line was set to 0.25 mm. To bind the patch substrate to the feed line substrate, the bonding prepreg RO4450 was used and it had a height of 0.102 mm.

Copper was employed as material for the conductors in the antenna. For the copper thickness of the feed line, patch and ground surrounding the patch, 43 µm was chosen. The copper ground plane thickness in between the patch and feed line substrates was set to 18 µm. To connect the antenna to an input source, the Sub-Miniature Push-on Micro (SMPM) Male PCB Surface Mount Connectors was implemented [42]. These where chosen based on availability from Chalmers, and the PCB was designed to allow for soldered connections of these. Figure 3.1 illustrates the side view of the antenna where each layer is marked.

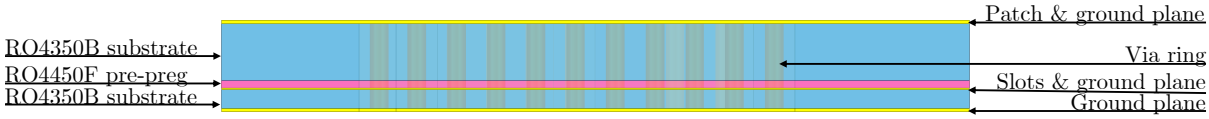

Figure 3.1: Profile view of the antenna.

3.1.2 Single-polarized Antenna

When designing a single-polarized antenna, the dimensions that had do be determined were: patch size, cavity size, microstrip size and slot size. The model was built in Ansys HFSS and wave ports were used to excite the feed lines in the beginning of the process. The connectors were first implemented when designing the array (explained in Section 3.1.5).

To achieve a resonance frequency at f_r, the length of the quadratic microstrip patch was estimated using Equation (2.29). The S_{11}-parameter was then analyzed using the SC in HFSS and the length was tuned to yield an optimal S_{11}-parameter in the frequency range $26.5 - 29.5$ GHz.

3.1.2.1 Designing the Slot

For calculating the width of the microstrip feed line, Equation (2.23) and (2.24) were used with the characteristic impedance Z_0 set to 50 Ω. The reason for 50 Ω is to match the impedance of the connectors and VNA. Thereafter, the characteristic impedance for the wave ports was analyzed in HFSS using the calculated width of the microstrip and then altered to achieve a value closer to 50 Ω.

To obtain optimal parameters for the slot, different values were investigated for the slot position, width and length. Figure 3.2 illustrates the different dimensions. The green box represents the patch, the blue the microstrip and the orange the slot in the ground plane. The distance between the patch center and the slot center is denoted with d.

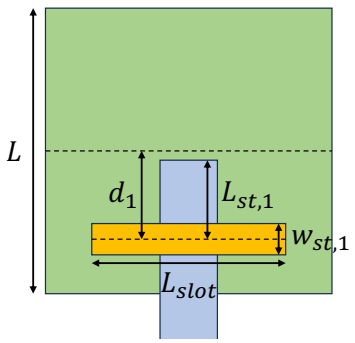

Figure 3.2: Illustration of the investigated parameters for the single polarized antenna element.

According to a numerical parametric assessment from [43], good performance was yielded with is a slot width of $0.05L - 0.2L$ and slot length of $0.2L - 0.8L$, where L is the patch length. These dimensions were used as rough guidelines when choosing which values to investigate. Table 3.3 presents the investigated parameters, where each combination was analyzed individually.

Table 3.3: The different slot dimensions that were tested for the single polarized antenna.

Parameter	**Values**		
d	0.3 mm	0.55 mm	0.8 mm
W_{slot}	$0.05L$	$0.1L$	$0.2L$
L_{slot}	$0.8L$	L	-

Another aspect that played in to the position of the slot was the possibility of implementing a second polarization in a later phase, hence a shorter distance than 0.3 mm was not investigated. The optimal combination was determined by studying the S_{11}-parameter in the SC. It was quickly concluded that a shorter length than $0.8L$ resulted in an undesired S_{11}-parameter, thus only longer lengths were studied. Further, the two analyzed slot lengths yielded quite similar result, which is the reason for not investigating a third value.

After testing the values mentioned above, further tuning was done by slightly adjusting the parameters until the S_{11}-parameter was satisfactory.

3.1.2.2 Impedance Matching Network

One of the performance targets in Table 3.1 is that the input reflection coefficient should be below -10 dB. This was the main objective when designing the single-polarized antenna. In the previous stages, the focus was on creating an adequate loop for the resonance frequency in the SC that would in turn be easy to shift close to the matching point (middle of SC) by impedance matching, see Section 2.5.2.

Studying the SC, it was concluded that the S_{11}-parameter was too inductive, therefore an open ended parallel stub was added. Further, the Circuit Design tool in HFSS calculated an electrical length for the stub, which was used as a first estimation. However, since the extra TL also introduces some induction, the length and width of the extra stub, as well as the position in relations to the slot, had to be tuned. The extra feed line after the slot, L_{stub1} in Figure 3.2, also impacted the reactivity. Consequently, it was tuned together with the extra stub.

3.1.3 Dual-polarized Antenna

After the target performance for the S_{11}-parameters was achieved for the single polarization, the second polarization was introduced. The aim for this stage was the polarization channel decoupling, where the S_{12}-parameter were to be below -15 dB. The channel decoupling were highly dependent on the proximity between the two slots. For that reason,

the decoupling was decreased by shifting the two slots together with the feed lines farther away from each other. In addition, the slot was bent to an U-shape to avoid intersection. Figure 3.3 depicts the position of the slots in relation to the patch. The added open ended stub was also shifted to avoid radiation leaking to the opposite slot. Moreover, to avoid collision between the stubs L_{stub1} shown in Figure 3.2, they were bent with a corresponding edge chamfer.

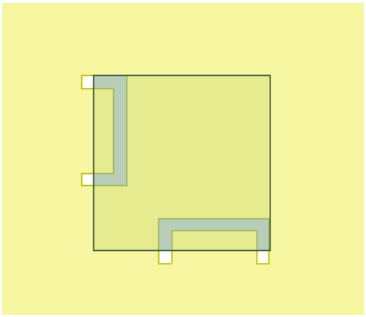

Figure 3.3: The slot positions relative to the patch for a dual-polarized antenna element.

All the alterations mentioned above resulted in changed S_{11}-parameters as well. As a result, the impedance matching in this stage had to take both the S_{11}- and S_{12}-parameters into account. Furthermore, the antenna was cavity-backed in order to reduce surface waves as described in Section 2.6.4. This was implemented with a ring of vias. Figure 3.4 depicts the final design of the single antenna element, which was triplicated to create the array.

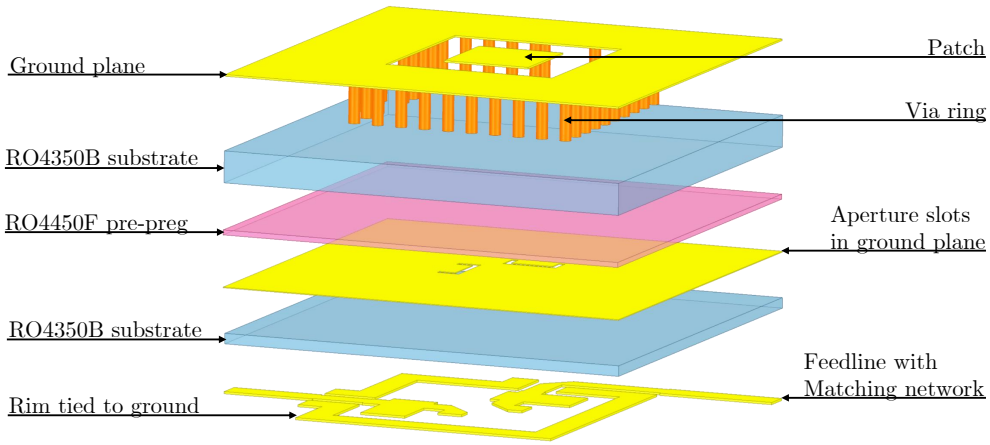

Figure 3.4: Layer overview of the single antenna element.

3.1.4 Linear Array

The dual-polarized antenna mentioned in the previous section is the completion of a single antenna element. To then make a linear array of it, three identical elements where placed in a line as seen in Figure 3.5.

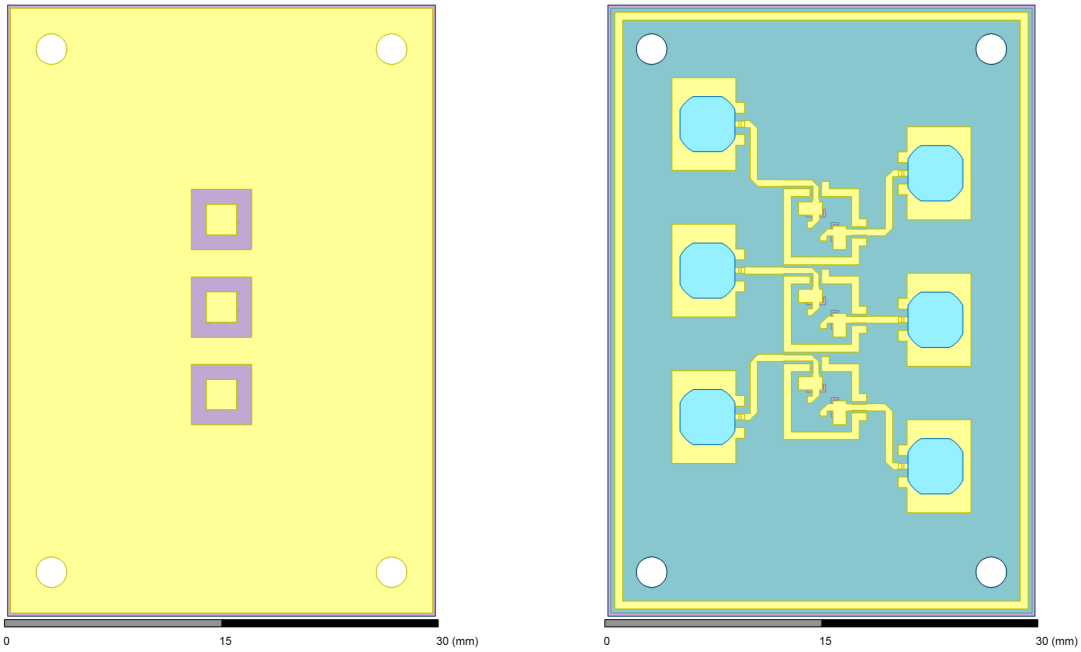

Figure 3.5: Render of the finished 1x3 linear array where. The left image shows the patch side and the right image the connector side.

For this implementation, two aspects had to be taken into account. The first being that to avoid grating lobes each element should not be spaced more than 0.5λ from each other, see Section 2.4.2.1. This in turn puts a constraint on how big each element is allowed to be. The second aspect relates to the microstrip lines that feeds the patch antenna. Because of the close proximity of each element, a section from three feed lines will be close to the cavity walls, see Figure 3.6. This introduces a disturbance that was taken into account for by making the affected parts of the microstrip thinner in width until the desired impedance of 50 Ω was achieved. The connectors where then spaced accordingly to ensure that all coaxial cables would fit. Finally, to reduce unwanted interference, a ring of vias was placed around the edge of the PCB.

Figure 3.6: Close-up view of the feed line and matching network for the horizontal polarization. The numbers describes the width of the microstrip line.

3.1.5 Implementing Connectors

Up until now the antenna simulations used the HFSS wave port for its excitation. This port can not be implemented outside of the simulation environment. To get a better insight in how the final antenna will behave, the wave port was replaced with the HFSS model for the actual connector used. A render of the connector can be seen in Figure 3.7. The connector has two contact points. The first being ground and the second being the feed line. In order to make the connector work as intended, it had to be impedance matched to the microstrip feed line. The impedance matching was done by adjusting the width of the feed line, where the arrows point at in Figure 3.7.

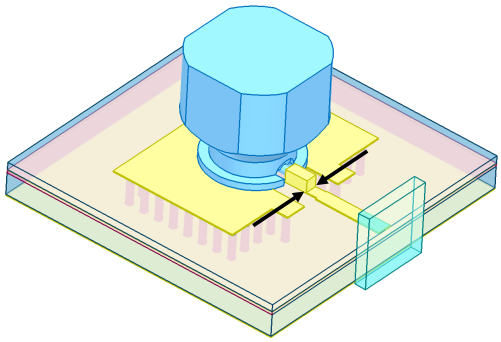

Figure 3.7: Render of the SMPM connector during its impedance matching.

The implementation of connectors could result in more losses compared to using wave ports in HFSS. Partly due to imperfect impedance matching and partly because of the extra TL to the connectors and the insertion loss of the connector. The reason for extra TL was to provide a fan-out and ensure enough connector-to-connector spacing to fit the adapters and terminators when testing. Hence, the effects of the connectors were evaluated by comparing the results of the gain from the final array with a similar array but with wave ports instead. The model is presented in Figure 3.8.

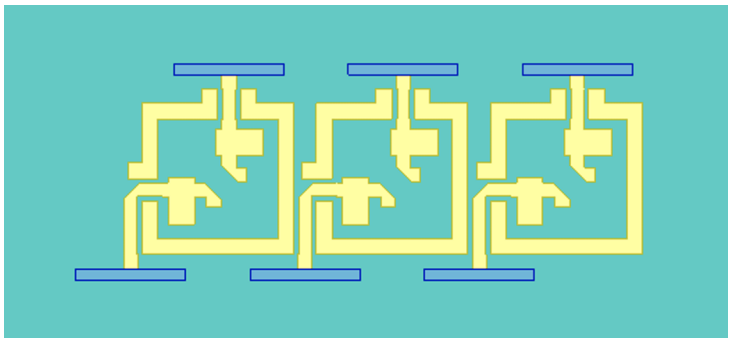

Figure 3.8: Render of the antenna array using wave ports instead of SMPM connectors.

3.2 Manufacturing

Keysight ADS was employed to generate the Gerber and drill files. The reason being that the software provided an efficient layout environment compared to Ansys HFSS. This transition from Ansys HFSS to Keysight involves a 2D view of each layer through DXF import/export, with specific dimensions which fulfill the requirements of the product. Then the files were sent to Eurocircuits for PCB manufacturing.

3.3 Testing and Verifying

Following the simulation phase, physical tests were carried out on the fabricated antenna array. During testing, two primary types of measurements were conducted: S-parameters and radiation patterns (realized gain). A comparison between measured results and simulated data was conducted, to determine if the fabricated antenna design met the specific requirements mentioned in Section 3.1.1.

3.3.1 Scattering Parameters Measurements

S-parameters were measured by utilizing the vector network analyzer (VNA). It measures the incident and the reflected voltage wave at its ports, yielding the S-parameters. In this setup, seen in Figure 3.9b, the ports of the antenna were tested in pairs. Since a 2-port VNA was employed for a 6-port antenna, only two ports could be active simultaneously. To prevent the unwanted reflection from inactive ports from affecting the measurements, 50 Ω, terminators where attached to the passive ports. This ensure that measurements for the active ports remained accurate.

Due to the SMPM connectors mounted closely, the VNA cables were too large to be plugged in at the same time. Therefor an additional thinner cable was also used in the measurement setup. Simultaneously the other port was linked to a metal 2.4-to-SMPM adapter as illustrated in Figure 3.9a, which was necessary to establish the connection between the antenna and VNA. However, it is important to note that this additional cable introduced a loss of 1 dB. To enhance accuracy, internal losses were measured and subsequently excluded from the measured values.

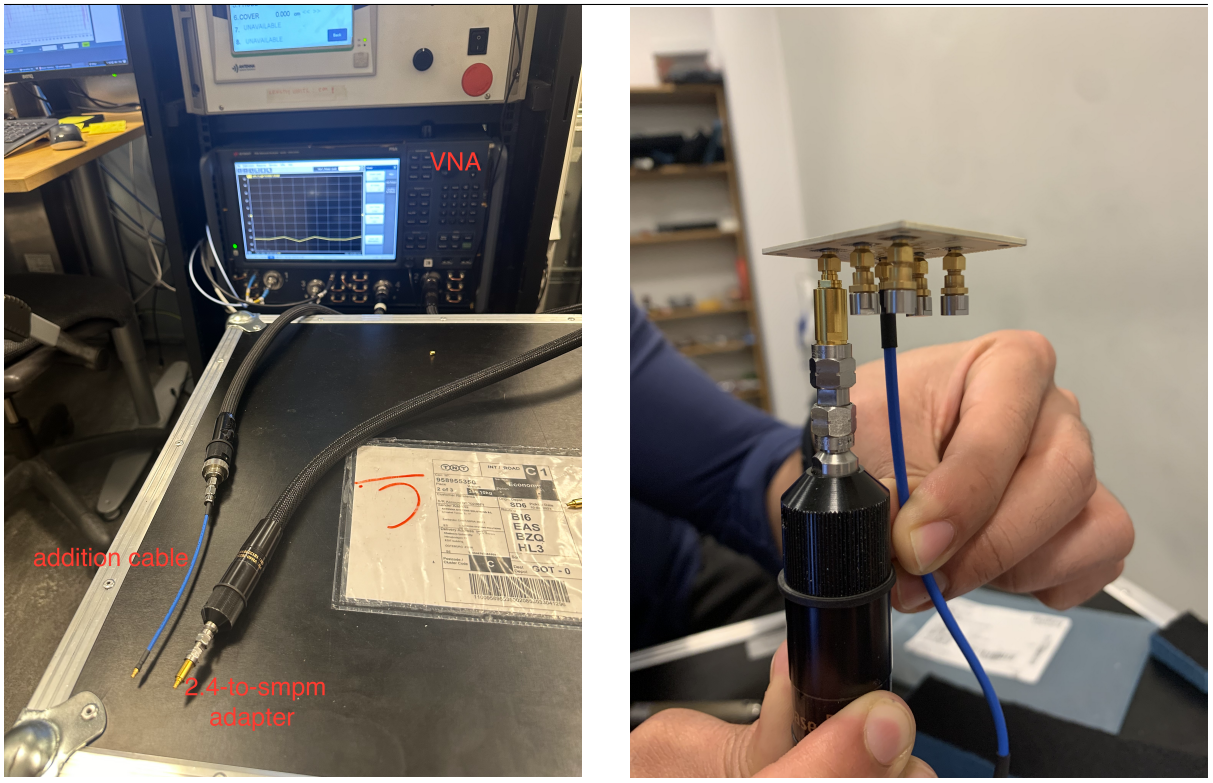

(a) VNA, cable and adapter.

(b) The antenna array with terminators.

Figure 3.9: Depiction of the instruments used during S-parameter measurements.

3.3.2 Radiation Pattern Measurements

The far-field setup was applied to get the measurements of the radiation pattern in the Chalmers terahertz anechoic chamber, which can be seen in Figure 3.10. A printed plastic adapter was designed in Autodesk Fusion 360 and used to mount the antenna array on the antenna mast as seen in Figure 3.11a. Furthermore, a carbon-loaded polyurethane foam was placed around the antenna to suppress backward radiation caused by the slot and feeding circuit but also to cover the metal stand, which is depicted in Figure 3.11b. A receiving antenna measured the radiated field from the antenna under test (AUT) at various angels, by rotating the mast. To calculate the realized gain, a standard gain horn (SGH) antenna with known characteristics was used as a reference. To obtain the shape of the radiating pattern the same procedure was carried for one antenna port at a time, while the others were terminated with loads. Hence, the realized gain for each antenna element was obtained. To compensate for the cable loss 1 dB was added to the results in post-processing.

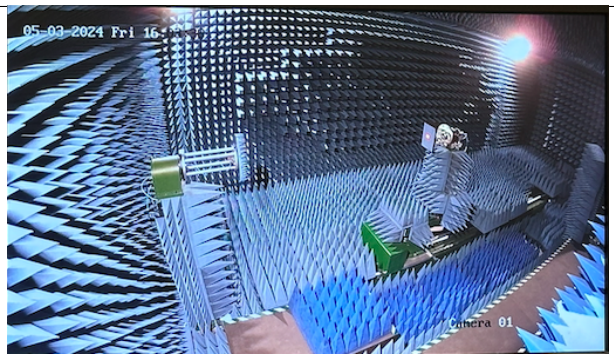

Figure 3.10: Chalmers terahertz anechoic chamber.

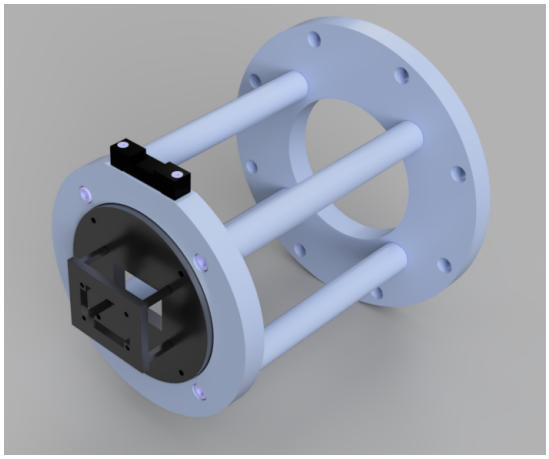

(a) 3D printed adapter (black part).

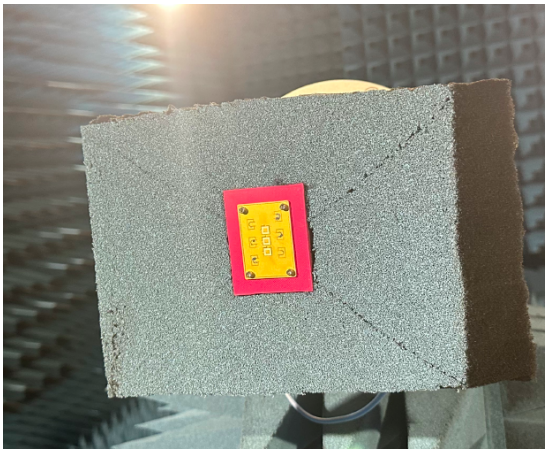

(b) Antenna mast surrounded by foam.

Figure 3.11: Attachments used for tests in the anechoic chamber.

3.3.3 Total Efficiency Measurements

The total efficiency was measured using a reverberation chamber. Only the center antenna element was measured, for both V- and H-polarization. The other ports were terminated. Further, a SGH was used as reference antenna to calibrate the instruments. First, the SGH was excited with the AUT inside the chamber at the same time, but completely terminated. The purpose was to measure chamber loss, which account for the physical space of the AUT and the antenna mount. Subsequently, the tests were carried out with the AUT excited and the SGH terminated. The setup is shown in Figure 3.12 with the AUT to the right and SGH to the left. Lastly, the losses of the cables were estimated to contribute with 1 dB, which was compensated for in post-processing. As for the total efficiency from the simulated antenna they where extracted from HFSS antenna parameters.

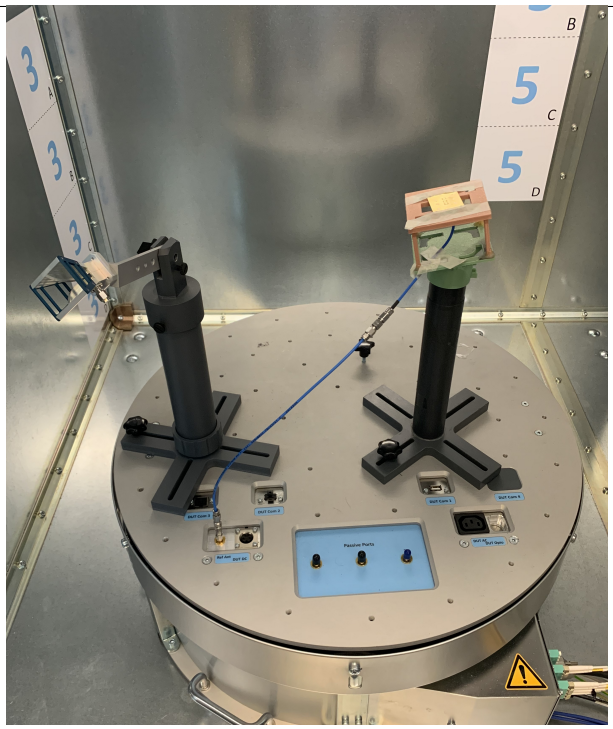

Figure 3.12: Setup of the reverberation chamber.

3.4 Beam Steering

The beam steering was studied for both polarizations (vertical and horizontal) and with three different frequencies: 26.5, 28 and 29.5 GHz.

According to the Equation (2.16) the maximum beam steering angle is unaffected by the polarizations but varies with frequency (due to the λ-dependence). To confirm these calculations, the finalized array was simulated in HFSS and the magnitude and phase of the normalized co-polarized E-field was plotted in the $\phi = 90°$-plane. The reason for choosing $\phi = 90°$ was because the array was aligned along the y-axis ($\phi = 90°$). In order to visualize how different phase shifts would affect the main beam, the radiated E-field from the antenna structure had to be extracted for each port separately and then summed in a MATLAB script, where the phase shift could be altered effectively. Moreover, the phase shift was calculated using the conjugate of each elements E-field for the corresponding scan angle θ, as described in Section 2.4.2.

Using Equation (2.7) together with (2.3), the following formula was derived for the power gain

$$G = \frac{4\pi R^2 |\mathbf{E}^{\text{co}}(R,\theta,\phi)|^2}{2\eta_0 P_{\text{in}}} = \{\eta_0 = 120\pi\} = \frac{|R\mathbf{E}^{\text{co}}(R,\theta,\phi)|^2}{60 P_{\text{in}}}. \tag{3.1}$$

Depending on which port was excited, the normalized co-polarized E-field for the $\phi = 90°$-plane is either θ or ϕ oriented. For the vertical polarization, the normalized co-polarized E-field is RE_ϕ, while it is RE_θ for the horizontal polarization. For the cross-polarized

E-field, the opposite applies. By employing Equation (3.1) on the exported RE_ϕ and RE_θ-values, the gain was calculated for $\theta = (-90...90)^\circ$.

Moreover, the main lobe was plotted for the realized gain G_r, which takes into account losses from mismatching and MC. This was accomplished by applying Equation (3.1), where instead of utilizing the accepted input power P_{in}, the supplied power P_{s} to the ports was used. Each port was excited with 1 W, hence the total supplied power was 3 W.

The beam steering was also investigated for the measured data in a similar manner. However, the radiation pattern obtained from the anechoic chamber were given as realized gain instead of normalized E-field. In order to evaluate and compare the beam steering capabilities of the measured and simulated data, the scan angle was used as a figure of merit. The scan angle was defined as the θ-value of which the realized gain was 3 dB lower than the peak broadside gain.

4

Results

In this section both the simulated results from Ansys HFSS and the measured results from the physical antenna are displayed. The presentation will start with the dimensions of the final antenna design and thereafter the performance figure of merits.

4.1 Final Design

Figure 4.1 shows the bottom view of the final design of a single antenna element. The values of the dimensions marked in the figure, together with the dimensions depicted in Figure 3.2, are presented in table 4.1.

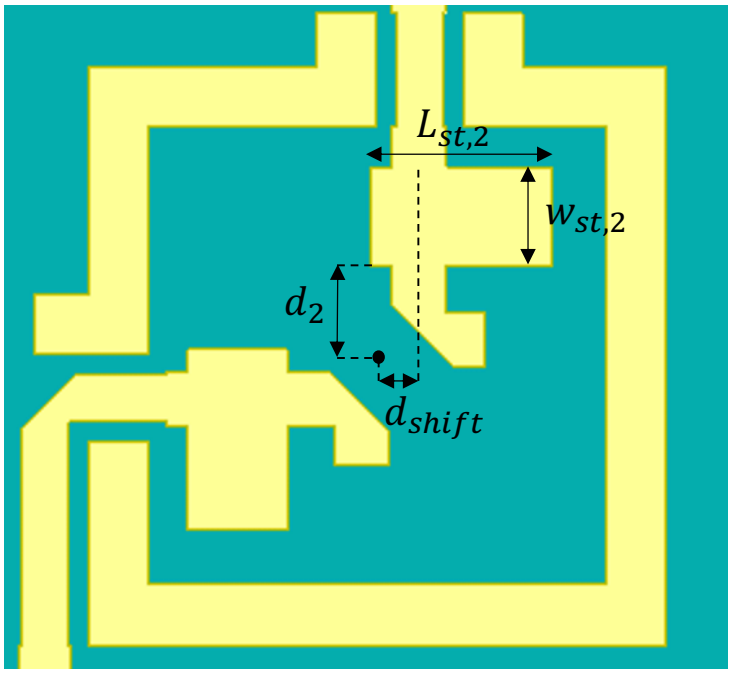

Figure 4.1: Dimensions for the impedance matching of the single antenna element design.

Table 4.1: Parameters of the final design of the single antenna element.

Parameter	Entity	Value (mm)
Slot length	L_{slot}	1.83
Slot width	w_{slot}	0.15
Distance from slot to center of patch	d_1	0.750
First stub length	$L_{\text{st},1}$	0.591
First stub width	$w_{\text{st},1}$	0.498
Second stub length	$L_{\text{st},2}$	1.66
Second stub width	$w_{\text{st},2}$	0.920
Distance from stub to center of patch	d_2	0.825
Distance shifted from center of patch	d_{shift}	0.4
Patch size	L	2.13

The width of the microstrip lines is presented in Figure 4.2.

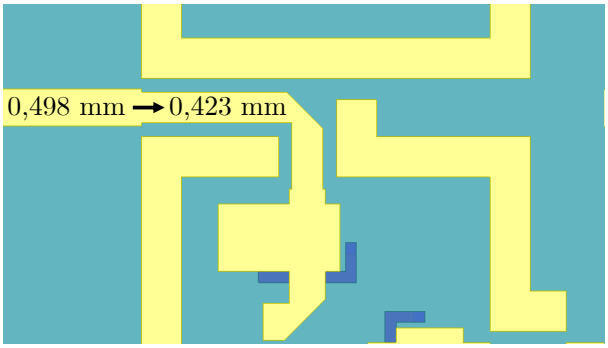

Figure 4.2: Close-up view of the feed line and matching network for the horizontal polarization. The numbers describes the width of the microstrip line.

Furthermore, the parameters for the final design of the array are presented in Table 4.2.

Table 4.2: Parameters of the final design of the antenna array.

Parameter	Value (mm)
Distance between adjacent elements (center to center)	6.13
Distance between adjacent connectors (edge to edge)	6.41
PCB length	42.4
PCB width	29.6

A picture of the manufactured antenna array can be seen in Figure 4.3.

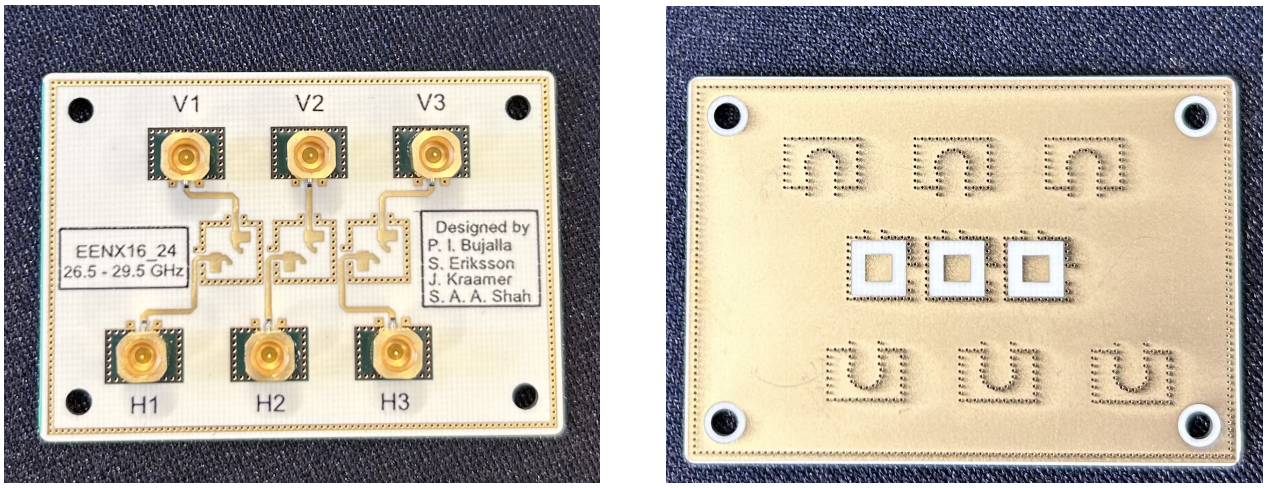

(a) Bottom view (connector side). **(b)** Top view (patch side).

Figure 4.3: The manufactured final design of the antenna array.

4.2 Performance

The result of the performance begins with the S-parameters and realized gain for the radiation pattern. Firstly, the radiation pattern is illustrated for simulated values of the SIE. Since the SIE was not manufactured, it does not have any measured results. For the EEP, both the measured and simulated value are presented. Lastly, the chapter moves on to total efficiency, beam steering and ends with a summary of the target metrics. It should be noted that for all realized gain plots and efficiency plots the measured values are post-processed with a smoothing function (*smoothdata()*) in MATLAB to reduce the ripples.

4.2.1 Scattering Parameters

Presented in this section are the results from measured and simulated S-parameters of the antenna array, see Section 2.2.3 for explanation of S-parameters. The ports of the antenna will be referred to as S_{ij}, where i, j are representing the corresponding ports seen in Table 3.2. How the port are placed can be seen in Figure 4.3a. All plots of the S-parameters presented in this section relate to the center element. The remaining S-parameters are shown in Appendix A.

First, the input reflection coefficients of the middle antenna element are displayed in Figure 4.4 and 4.5, in the form of SC and dB-plot respectively.

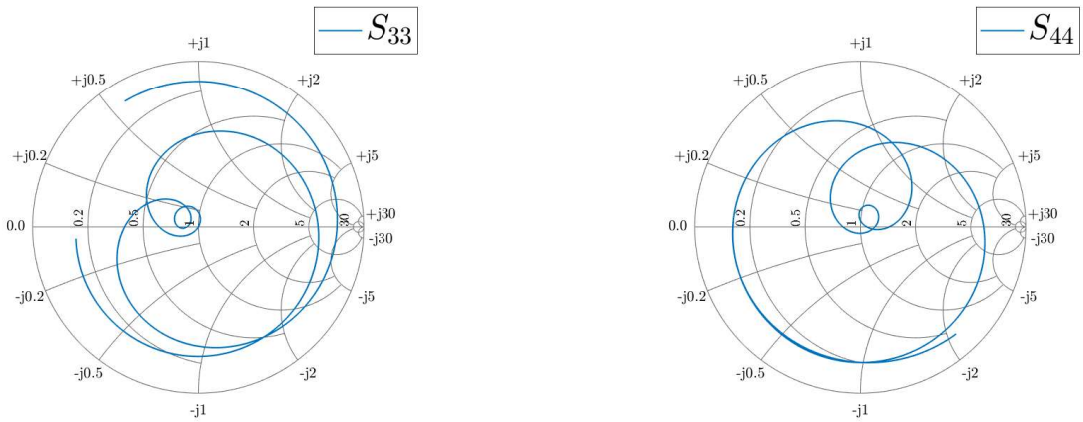

(a) S_{33}. **(b)** S_{44}.

Figure 4.4: Smith chart of simulated input-port reflection coefficients for the center antenna element of the array.

Notable in the SC for the input port reflection coefficients for the horizontal, S_{33}, and for the vertical, S_{44}, port is that the curves has a loop close to the center of the chart. These loops contains the frequencies of the 5G NR 257 band and the close proximity of the loops in regard to the center indicates that the antenna should have a good performance within these frequencies.

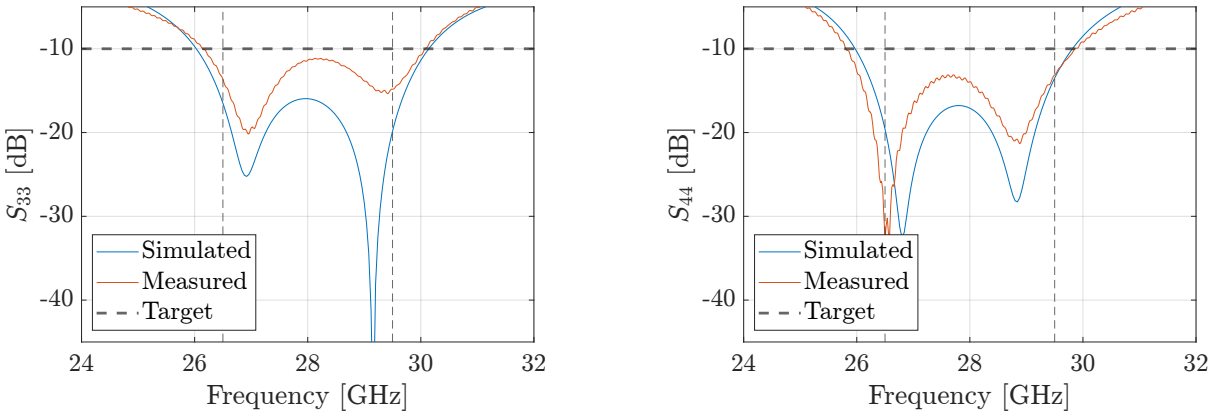

(a) S_{33}. **(b)** S_{44}.

Figure 4.5: Simulated and measured input reflection coefficients for the center antenna element.

The self-coupling coefficients for the simulated and measured antenna are depicted in Figure 4.6.

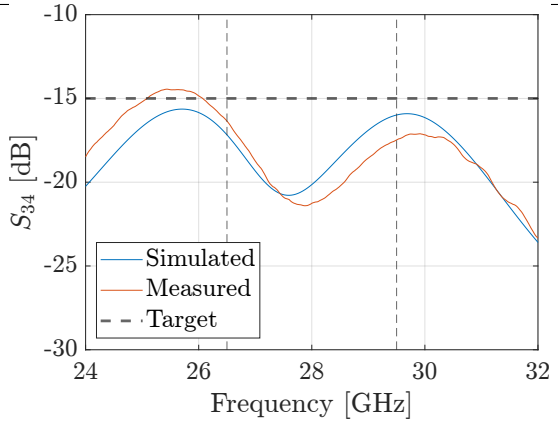

Figure 4.6: Simulated and measured polarization self-coupling coefficient, S_{34}, for the center antenna element.

Co-polarized mutual coupling is presented in Figure 4.7.

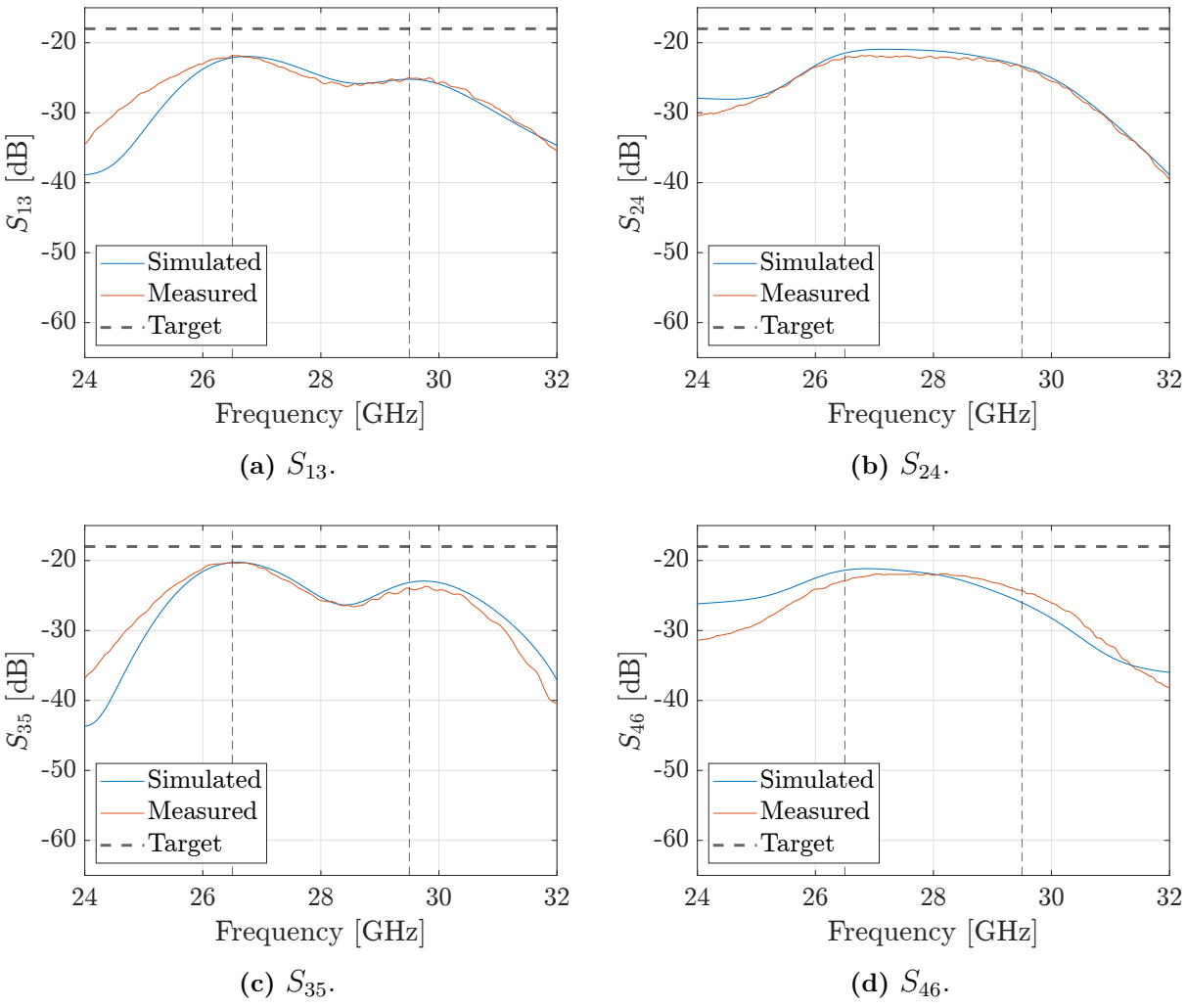

(a) S_{13}. **(b)** S_{24}.

(c) S_{35}. **(d)** S_{46}.

Figure 4.7: Simulated and measured co-polarized element mutual coupling coefficients.

The result of cross-polarized MC for the measured and simulated antenna array are illustrated in Figure 4.8.

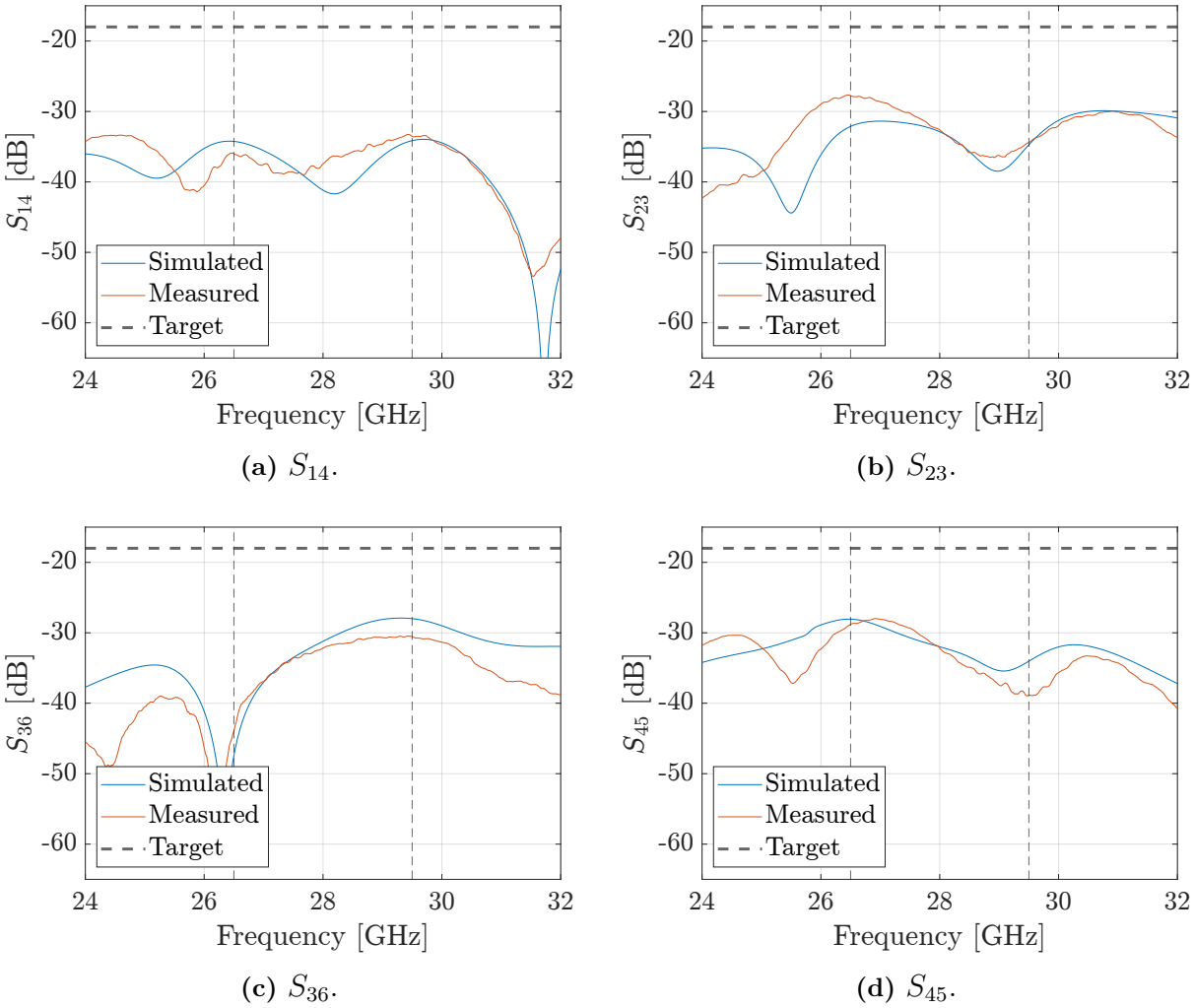

(a) S_{14}. **(b)** S_{23}. **(c)** S_{36}. **(d)** S_{45}.

Figure 4.8: Simulated and measured cross-polarized element mutual coupling coefficients.

4.2.2 Single Isolated Element

Figure 4.9 and 4.10 shows the simulated realized gain for a single antenna element. The patch was excited with wave ports in HFSS, instead of connectors. The results for the lower and upper frequency limit (26.5 GHz and 29.5 GHz) are presented in Appendix B.

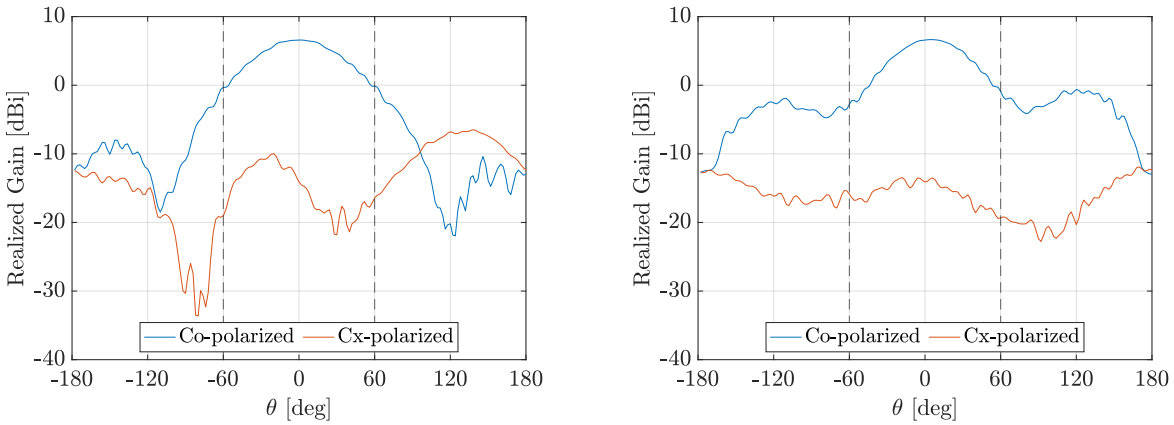

(a) $\phi = 0°$. **(b)** $\phi = 90°$.

Figure 4.9: Simulated realized gain for a H-polarized single isolated element at 28 GHz.

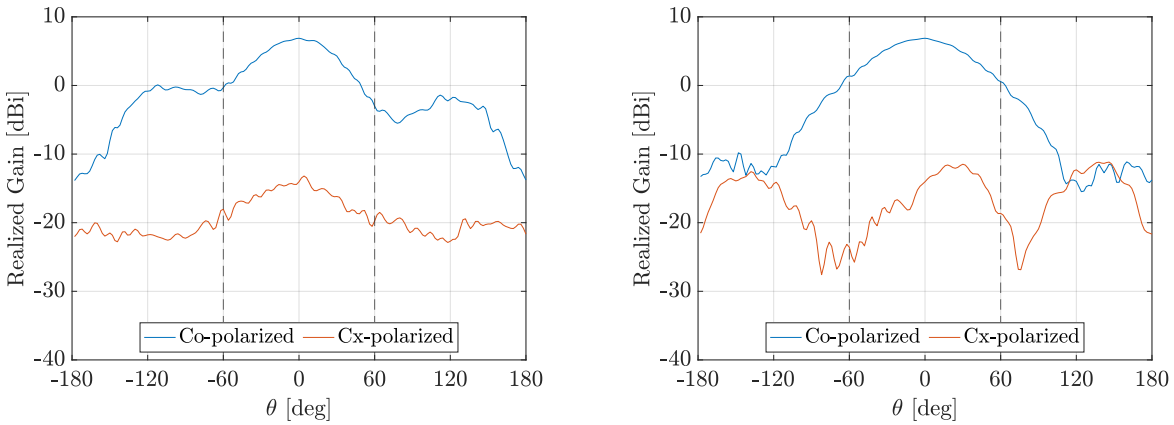

(a) $\phi = 0°$. **(b)** $\phi = 90°$.

Figure 4.10: Simulated realized gain for a V-polarized single isolated element at 28 GHz.

The target for the angular coverage was ±60°. Table 4.3 presents the angular coverage for each port at 28 GHz. The coverage is defined as the θ-angle where the realized gain is 6 dB below the peak broadside gain.

Table 4.3: Angular coverage for the single isolated element at 28 GHz.

Port	**Plane $\phi = 0°$**	**Plane $\phi = 90°$**
V-polarized	±50°	±56°
H-polarized	±54°	±48°

4.2.3 Embedded Element Pattern

Figure 4.11 and 4.12 depict the radiation patterns for the measured and simulated antennas at 28 GHz for two different planes: $\phi = 0°$ and $\phi = 90°$. The results for the lower and upper frequency range are presented in Appendix C

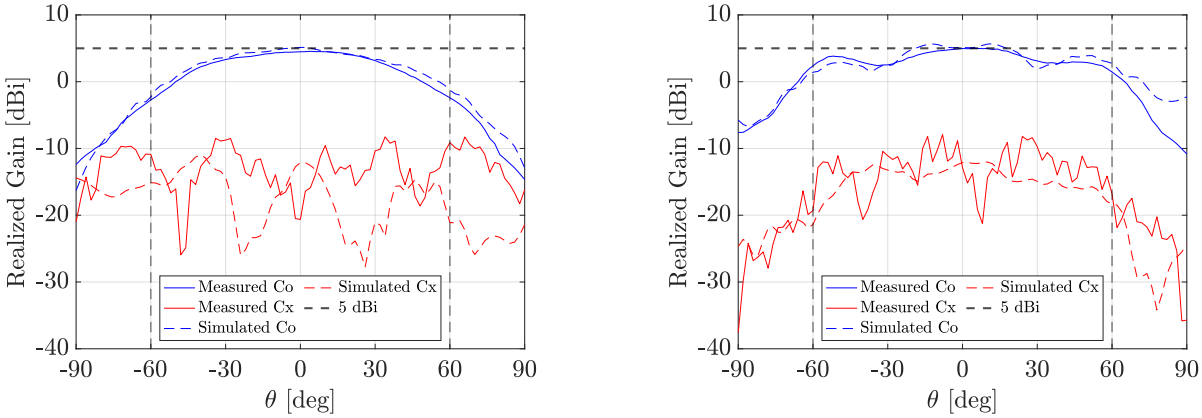

(a) $\phi = 0°$. **(b)** $\phi = 90°$.

Figure 4.11: Realized gain for the H-port of the center element (H2).

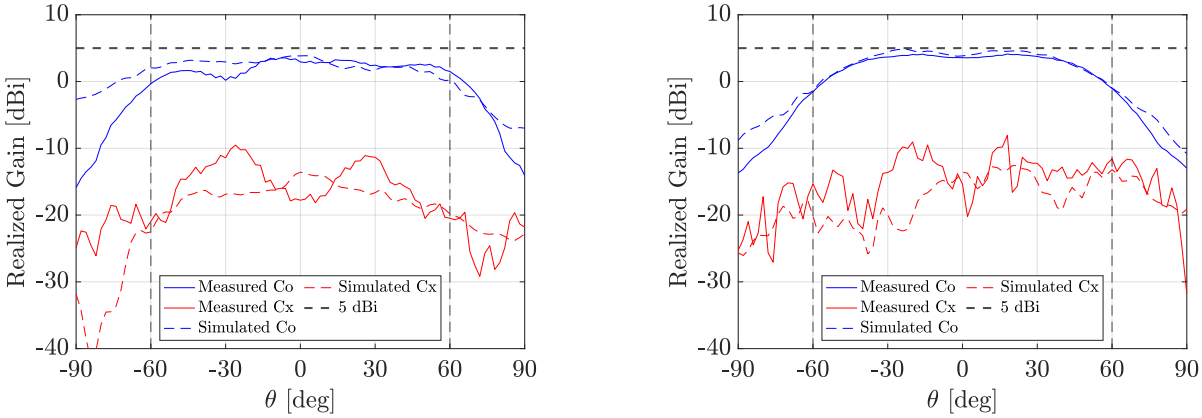

(a) $\phi = 0°$. **(b)** $\phi = 90°$.

Figure 4.12: Realized gain for the V-port of the center element (V2).

There was no specific target for the EEP, but the 5 dBi gain is marked in the plots for easier comparison with the SIE.

4.2.3.1 Losses from Connector Implementation

Table 4.4 presents the difference in peak broadside gain between two versions of the simulated array. One utilizing connectors and one wave port, as describes in Section 3.1.5. The peak broadside gain was higher when wave ports were used.

Table 4.4: Losses in peak broadside realized gain when each port was excited separately.

Port	Loss (dB)	Port	Loss (dB)
V1	1.3	H1	0.82
V2	0.70	H2	0.39
V3	1.4	H3	1.2

4.2.4 Total Efficiency

The plots in Figure 4.13 describe the total efficiency over the frequency range 26 to 30 GHz. The measured data is from the reverberation chamber whilst the simulated is exported from Ansys HFSS. It should be noted that the measured data from the reverberation chamber was very ripply due to a limited number of chamber stirrer positions, which affects the data averaging at mm-wave frequencies. To estimate the efficiency data, the *polyfit()* function in MATLAB was applied in post-processing. The polynomial curve fitting was set to five degrees. Moreover, the simulated radiation efficiency was also plotted to give better insight, given that the simulated total efficiency lacked data points.

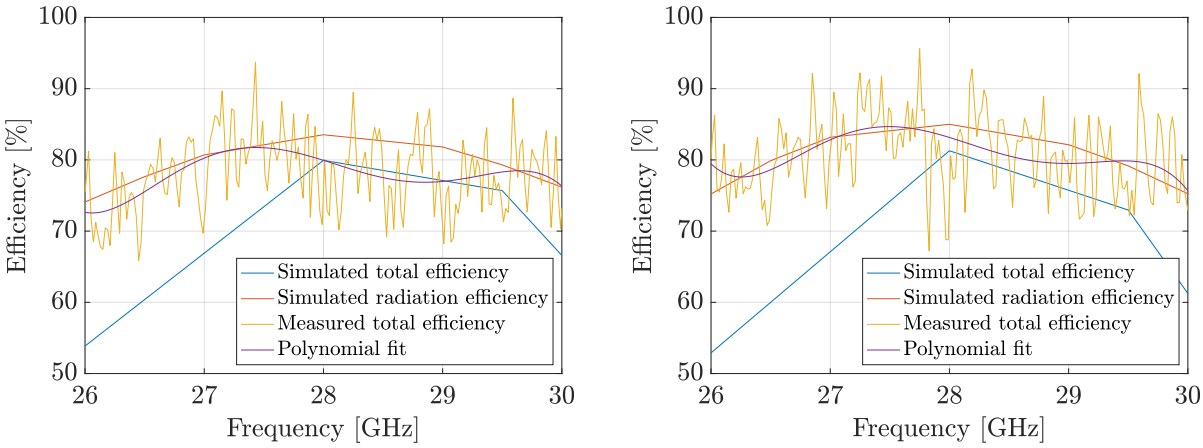

(a) Horizontal polarization (H2). **(b)** Vertical polarization (V2).

Figure 4.13: Simulated and measured total efficiency for each polarization of the center element.

4.2.5 Beam Steering

Figure 4.14 showcases the simulated beam steering capability of the antenna array at the frequency 28 GHz. Further, the beam steering from the measured data is illustrated in Figure 4.15.

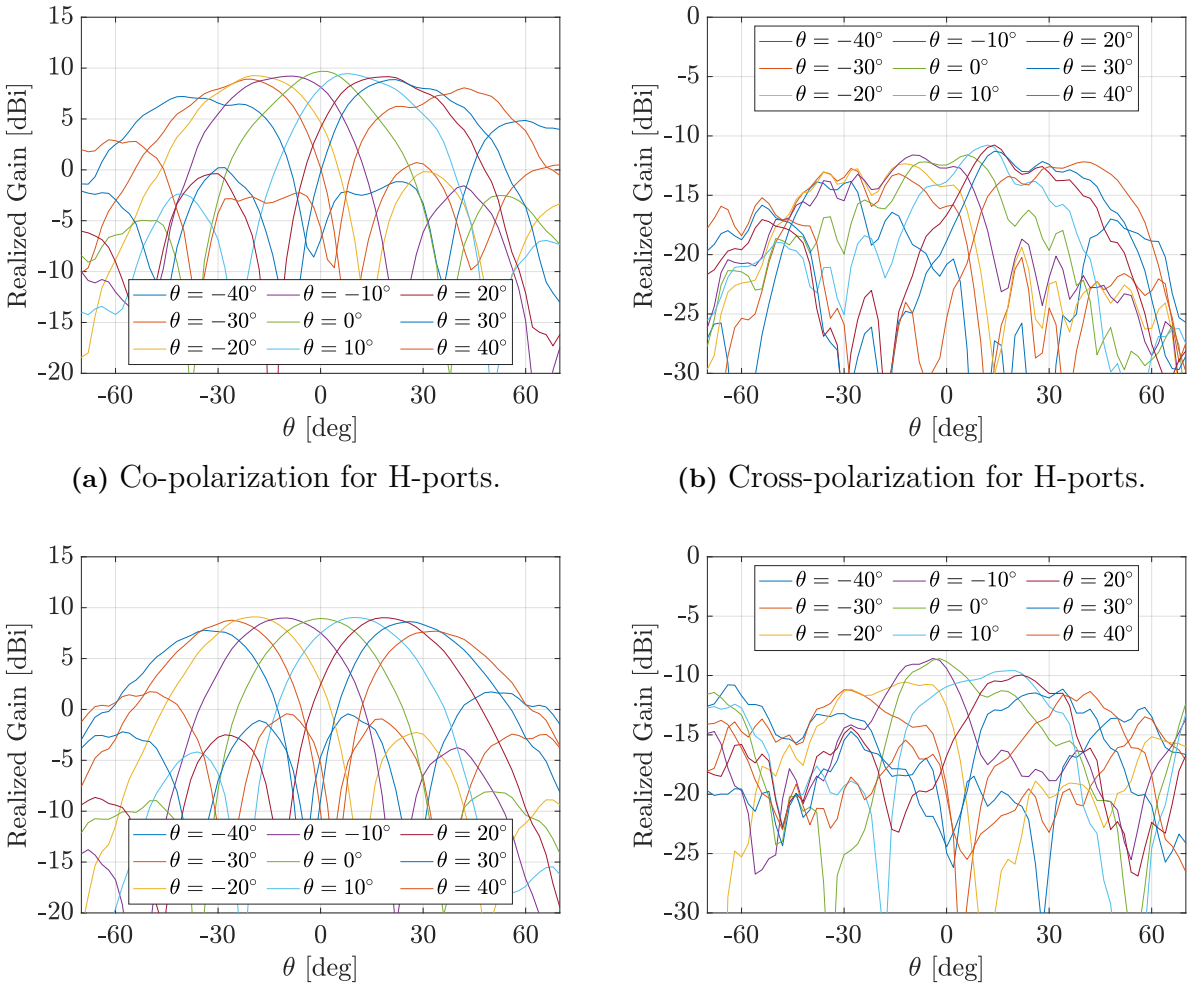

(a) Co-polarization for H-ports.

(b) Cross-polarization for H-ports.

(c) Co-polarization for V-ports.

(d) Cross-polarization for V-ports.

Figure 4.14: Beam steering of simulated values for the antenna array at 28 GHz.

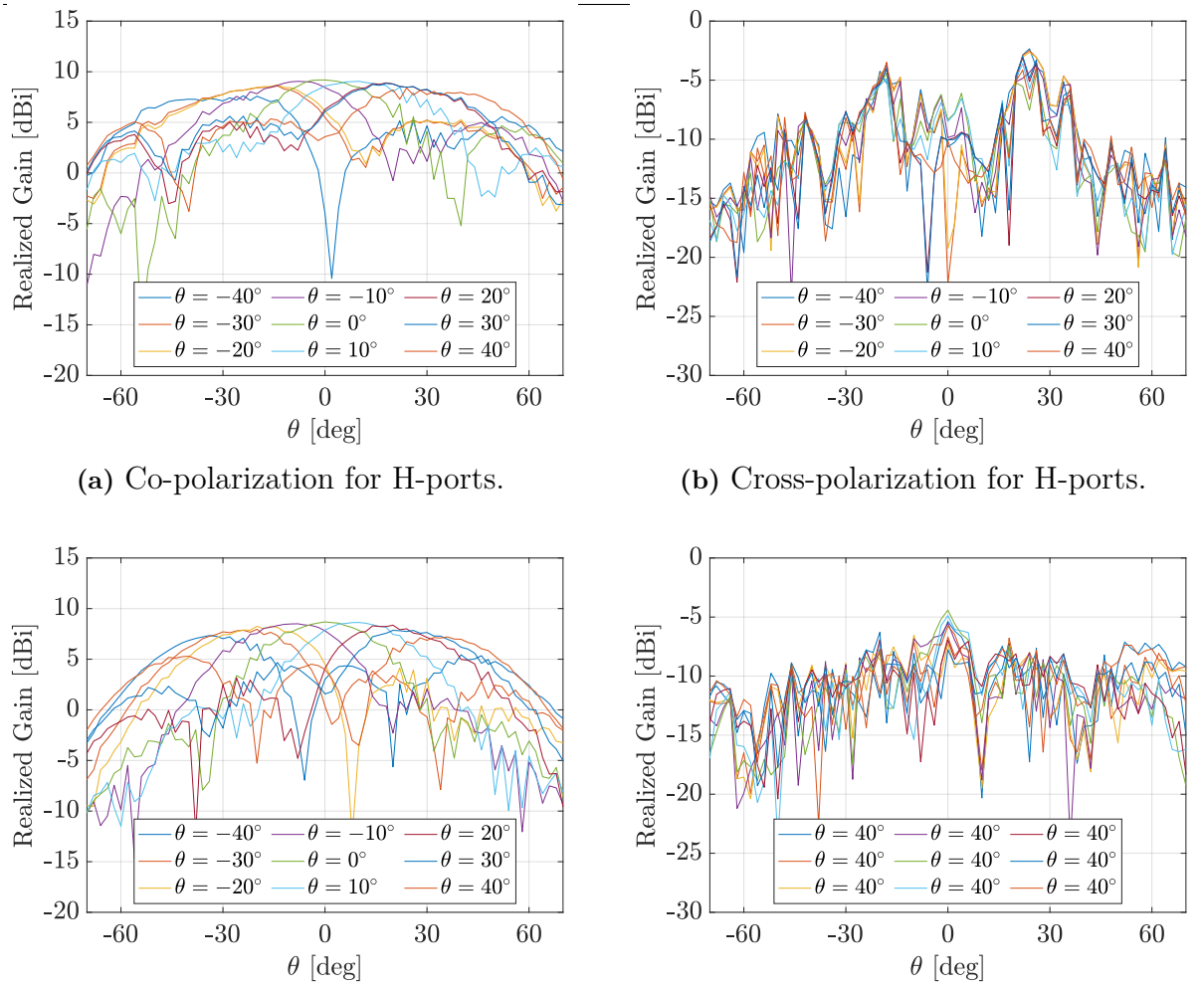

(a) Co-polarization for H-ports.

(b) Cross-polarization for H-ports.

(c) Co-polarization for V-ports.

(d) Cross-polarization for V-ports.

Figure 4.15: Beam steering of measured values for the antenna array at 28 GHz.

Table 4.5 summarizes the values obtained from the beam steering plots. Moreover, it considers only the co-polarization, since that determines the scan angle.

Table 4.5: Realized peak gain and scan angle for both V-polarized and H-polarized ports at 28 GHz.

Simulated/Measured	Port	Realized gain at $\theta = 0°$	Scan angle
Simulated data	V-polarized	8.9 dBi	±44°
Measured data	V-polarized	8.7 dBi	±46°
Simulated data	H-polarized	9.7 dBi	±44°
Measured data	H-polarized	9.2 dBi	±52°

Beam steering was also investigated for the band edge frequencies 26.5 GHz and 29.5 GHz. The plots for the co-polarized beam steering are displayed in Appendix D. The scan angle at 26.5 GHz was ±48° and ±60° for V- and H-polarized ports respectively. At 29.5 GHz the scan angle was ±40° and ±30° for V- and H-polarized ports respectively.

4.3 Results Compared to Target Performance

The following tables compare the target performance with the result. Table 4.6 gives an overview of parameters that were both simulated and tested. The values were derived from the plots of the S-parameters and total efficiency.

Table 4.6: A comparison between the measured and simulated results and if they reach the target performance.

Metric	**Target**	**Simulated**	**Measured**	**Achieved?**
Input reflection coefficients	< -10 dB	< -13.1 dB	< -11.3 dB	Yes
Polarized self-coupling coefficients	< -15 dB	< -16 dB	< -16.4 dB	Yes
Cross-polarized mutual coupling coefficients	< -18 dB	< -27.9 dB	< -27.9 dB	Yes
Co-polarized mutual coupling coefficients	< -18 dB	< -20.3 dB	< -20.3 dB	Yes
Total efficiency V-ports	$> 70\%$	$> 60\%$	$> 79\%$	Yes
Total efficiency H-ports	$> 70\%$	$> 60\%$	$> 75\%$	Yes

Moreover, Table 4.7 focuses on the SIE and how it compares to the target values, which were derived from Section 4.2.2. Since the SIE was not manufactured, only the simulated values are presented.

Table 4.7: Summary of the simulated results for the SIE and if they reach the target performance.

Metric	**Target**	**Plane $\phi = 0°$**	**Plane $\phi = 90°$**	**Achieved?**
Peak broadside gain V-ports	> 5 dBi	6.88 dBi	6.88 dBi	Yes
Peak broadside gain H-ports	> 5 dBi	6.58 dBi	6.58 dBi	Yes
Non-uniformity for angular coverage $\pm 60°$ V-ports	< 6 dB	9.89 dB	6.32 dB	No
Non-uniformity for angular coverage $\pm 60°$ H-ports	< 6 dB	6.88 dB	9.36 dB	No
Cross-polarized discrimination efficiency V-ports	> 10 dB	> 19.9 dB	> 16.3 dB	Yes
Cross-polarized discrimination efficiency H-ports	> 10 dB	> 15.5 dB	> 14.6 dB	Yes

5
Discussion

The following chapter focuses on how the measured and simulated values compare to each other and if they deviate from the target performance. Moreover, the beam steering capabilities are evaluated and some general improvements for the array are suggested.

5.1 Scattering Parameters

All plots of the S-parameters displayed in Section 4.2.1, as well as Appendix A, show that the target performance for input reflection coefficients, polarized self-coupling coefficients and MC coefficients are achieved. This applies to both simulated and measured values.

The input reflection coefficients indicates how much of the input power gets reflected back from the AUT (see Section 2.2.3). As both the results from the simulation and tests showed a value lower than -10 dB, this would mean that less than 10 % of the input power would be reflected back to the port. Moreover the self-coupling coefficients represent how much the two ports connected to the same antenna element influence each other. Since the ports are orthogonal, these S-parameters reveal the impact of cross-polarized radiation within one antenna element. The target of < -15 dB was achieved, which suggest that the polarization purity is retained, as mentioned in Section 2.3.

The target for co-polarized and cross-polarized MC of < -18 dB was also accomplished. A low co-polarized MC indicates adequate isolation between antenna elements when they are transmitting or receiving signals of the same polarization. Furthermore, low cross-polarized MC suggest that two different polarizations between elements are distinct from one another.

Simulated and measured data have minor deviation, with a plausible cause being the additional cable connected to the AUT, as seen in Figure 3.9. The additional cable was attached due to spacing limitations between the connectors, attached to the PCB, not allowing for direct connections with the two calibrated cables. The additional cable added was matched to 50 Ω. This addition has a similar affect as adding additional TL. It could cause differences in phase-shifts and amplitude due to losses. This additional cable could also explain the ripples displayed in the figures for the different S-parameters. Another plausible contributor of these differences could be the connectors, which are further discussed in Section 5.3.

5.2 Radiation Pattern for Single Isolated Element

Designing the single isolated element (SIE) was a significant part of the project as it was the building block for the later created array.

Table 4.7 shows the performance of the SIE and if it reached the targets set for it. Here the non-uniformity for the 60° angular coverage is the only metric that did not reach its target of < 6 dB. In Figures 4.9 and 4.10 it is visible that there is radiation on the backside of the antenna (when $\theta > 90°$ and $\theta < -90°$). When studying the E-field in Ansys HFSS, it was seen that this back radiation comes from the slots. Therefore, if the slot is better tuned, it could have a positive influence in reaching this target.

Shown in Table 4.7, the peak broadside gain is 6.58 dB for its horizontal port and 6.88 dB for the vertical port, so there is a difference of 0.3 dB between the ports even though they ideally should have the same value. In regards to what has been said about gain, one port appears to have more losses than the other port. Figure 4.1 shows that the horizontal ports microstrip feed line has a bend. This bend induces more losses than if the feed line was kept straight, like it is for the vertical port. It is therefore very likely that this is the main cause to the difference in gain.

In Ansys HFSS it was also identified that radiation leaked out of the cavity where the microstrip enters. To reduce this, additional cavity walls were added to the opening as seen in Figure 4.1. The gain could be increased by enclosing the opening even more.

In regards to the cross-polarized discrimination for the SIE it turned out to exceed the target performance of > 10 dB as seen in Table 4.7. What this means is that the SIE has a high polarization purity between the ports. This purity indicates that the antenna could be applied in a MIMO system, since signals could be distinguished and transceived simultaneously.

5.3 Embedded Element Patterns

Analyzing the result of the radiation patterns in Section 4.2.3, it can be observed that the measured data follows the simulated data well for both planes $\phi = 0°$ and $\phi = 90°$. However, a notable deviation appears for larger θ-values. An example of this can be seen in Figure 4.12a. The plastic printed 3D adapter (as seen in Figure 3.11b) where the antenna was mounted, was slightly tilted. The misalignment could have more affect for larger angles and thus be one cause for the discrepancy between measured and simulated values.

Furthermore, another factor that may have contributed to these deviations, is back radiation from the antenna. There was a lack of shielding with carbon loaded polyurethane foam around the metal antenna mast, only a small piece of foam was allocated between the plastic adapter and the front metal plate of the mast, as shown in Figure 3.11b. Hence, radiation could have been scattered on the mast from the transmitting AUT,

resulting in the ripples that had to be smoothed out in post-processing. The reflection of back radiation could be another reason to why the gain is higher for the measured data compared to the simulated data at larger θ-angles.

When comparing the plots for the radiation pattern of the SIE and EEP, the peak broadside gain is lower for all EEP (most below 5 dBi). Besides the affect of MC, the additional circuitry that was added to the SIE introduced more losses. The circuitry consisted of a longer microstrip feed line and a connector. The connectors were installed to allow for easy testing of the antenna. If the connector is not perfectly matched to the microstrip line, this too will add to losses in the system and as a consequence also in gain. Furthermore, in order to fit the testing cables, the connectors had to be fanned out allowing space in between. Thus, the feed line to ports H1, V1, H3 and V3 were longer, which resulted in extra losses. The extra losses in gain can be seen in Table 4.4.

5.4 Total Efficiency

The total efficiency is the ratio of radiated power over the incident power and gives an insight in how power enters from the TL into free space. Figures 4.13a and 4.13b show the efficiency of the manufactured antenna and the simulated. Only the measured curve was above the target performance of 70 %. The simulated total efficiency did not reach the target. Due to time constrains, too few data points where gathered for it to be reliable at 26.5 GHz. If however it can be assumed that the total efficiency has the same curve characteristic as the radiation efficiency, the target most likely would have been achieved. To improve the reliability of the results, especially since the data is noisy, more measurements could have been conducted.

5.5 Beam Steering

The plots of the beam steering for different polarized ports in Section 4.2.5 suggest that it is possible to steer the main lobe by phase shifting the current into the antenna array. Moreover, the phase shifting allowed a high realized gain at $\theta = 0$ as presented in 4.5. The high realized gain is expected since the radiation pattern summarizes the gain for all antenna elements, compared to the gain plots for EEP in Section 4.2.3.

Table 4.5 also shows that the scan angles are the same for the simulated data for both polarizations. In contrast, the measured data suggests a broader scan angle and the polarizations differs with 6°. One possible explanation for the improved scan angle could be that the reflection of back radiation, as discussed above, yields a larger coverage for the measured EEP compared to the simulated.

It could be concluded from the simulated cross-polarization plots in Figure 4.14b and 4.14d that the gain remains low and is not much affected by the beam steering, which is desirable. In contrast, for the measured data (Figure 4.15b and 4.15d), the cross-polarization is above -5 dBi and could therefore negatively affect the clarity of the signal

in a communication setting, as proposed in Section 2.3.

One of the limiting factor for the beam steering is the appearance of grating lobes. The equation for calculating the maximum steering angle to avoid grating lobes is presented in Equation (2.15). The relation infers that a lower frequency, thus longer wavelength, would result in a larger beam steering angle. Since the beam steering at other frequencies showed that the scan angle was broader for 26.5 GHz compared to 29.5GHz, the result agrees with the theory. Furthermore, the maximum inter-element distance d for a $\pm 90^\circ$ scanning angle is $\frac{\lambda}{2}$. The designed array has $d = 0.57\lambda$ at 28 GHz, leading to a more narrow scan angle. A smaller d could hence improve the beam steering capabilities.

5.6 General Improvements

When designing the single antenna element, it was clear that the S-parameters and radiation pattern was deeply dependent on the dimensions and shape of the slot. Small alterations resulted in a large impact on the performance. Hence, to achieve all requirements such as non uniformity for the angular coverage, more slot shapes could have been investigated. The material selection and thickness for the substrates were predetermined, and the same material was used for both substrates, this due to supply concerns from the manufacturer. Substrate material and thickness have significant impact on the MPAs characteristics, as mentioned in 2.6.2. Allowing different materials for each substrate, with different ϵ_r and thickness, would allow for increased optimization possibilities of the MPAs performance. However, this approach of introducing additional parameters would have increased the complexity of the design process.

6
Conclusion

In summary, the purpose of the project was to design, manufacture and test a low-profile dual-polarized antenna for 5G mm-wave application (26.5 - 29.5 GHz). A printed circuit board (PCB) based microstrip patch antenna was designed, where the antenna consisted of three antenna elements in a linear array. Both the designed and tested antenna yielded low S-parameters and were well below the target level. Hence, the impedance matching for reducing the S-parameters was successful. The implication is that a fractional part of input power is lost in reflections and that the polarization coupling within one element as well as between elements is weak. Moreover, the measured and simulated S-parameters were similar, indicating that the manufactured antenna was accurate to the designed model.

The peak broadside gain of the vertical (V) port and horizontal (H) port were 6.9 dBi and 6.6 dBi for the simulated isolated element, which exceeds the target of 5 dBi. However, the target for the angular coverage was not met. The simulated data depicted a coverage of $\pm 48^{\circ}$ for the H-ports which is less than the target $\pm 60^{\circ}$. A plausible explanation is back radiation induced by the slot. The simulated realized gain for an element in the array was lower than 5 dBi, which could be due to connector losses. In contrast, the angular coverage was broader for the embedded element than the isolated. Likewise to the S-parameter, the measured values corresponded well with the simulated values. Furthermore, the measured total efficiency was $> 79\%$ for V-polarization and $> 75\%$ for H-polarization, meeting the target performance of $> 70\%$.

Beam steering is possible for both the measured and simulated data. The measured data had a larger scan range but lower peak realized gain than the simulated data. A potential cause is the back radiation, which may be reflected on the mount used in the anechoic chamber.

For future studies, the angular coverage could be improved by investigating different slot and patch shapes as well as other array constellation such as a planar (2x2) array instead of a linear.

References

[1] F. Shen, H. Shi, and Y. Yang, "A comprehensive study of 5G and 6G networks", in *2021 International Conference on Wireless Communications and Smart Grid (ICWCSG)*, 2021, pp. 321–326. DOI: 10.1109/ICWCSG53609.2021.00070.

[2] P. K. Rai, Chandan, A. K. Singh, and S. M. Shukla, "Low profile multiband meander strip monopole antenna for tv broad cost/5g mobile communication system/ wlan applications", in *2023 International Conference on IoT, Communication and Automation Technology (ICICAT)*, 2023, pp. 1–5. DOI: 10.1109/ICICAT57735.2023.10263697.

[3] R. Young, S. Fallon, P. Jacob, and D. O'Dwyer, "Vehicle telematics and its role as a key enabler in the development of smart cities", *IEEE Sensors Journal*, vol. 20, no. 19, pp. 11 713–11 724, 2020. DOI: 10.1109/JSEN.2020.2997129.

[4] P. J. Mateo, A. B. Pizarro, N. Ludant, *et al.*, "A comprehensive study of low frequency and high frequency channel correlation", in *2019 International Conference on Computing, Networking and Communications (ICNC)*, 2019, pp. 876–882. DOI: 10.1109/ICCNC.2019.8685565.

[5] P. S. Khodashenas, J. Aznar, A. Legarrea, *et al.*, "5G network challenges and realization insights", in *2016 18th International Conference on Transparent Optical Networks (ICTON)*, 2016, pp. 1–4. DOI: 10.1109/ICTON.2016.7550539.

[6] E. Dahlman, S. Parkvall, and J. Sköld, *5G NR: the Next Generation Wireless Access Technology*. Elsevier Science Technology, 2018, ch. 3, pp. 27–36.

[7] D. Pozar, "Microstrip antennas", *Proceedings of the IEEE*, vol. 80, no. 1, pp. 79–91, 1992. DOI: 10.1109/5.119568.

[8] C. A. Balanis, *Antenna Theory: Analysis and Design*. John Wiley & Sons, Inc., Hoboken, New Jersey, 2016.

[9] S. Padhi, N. Karmakar, C. Law, and S. Aditya, "A dual polarized aperture coupled circular patch antenna using a c-shaped coupling slot", *IEEE Transactions on Antennas and Propagation*, vol. 51, no. 12, pp. 3295–3298, 2003. DOI: 10.1109/TAP.2003.820947.

[10] R. T. Jacob, S. Muzahir Abbas, R. Salama, and R. Liyanapathirana, "Feed analysis of a proximity coupled microstrip patch antenna", in *2022 IEEE International Symposium on Antennas and Propagation and USNC-URSI Radio Science Meeting (AP-S/URSI)*, 2022, pp. 846–847. DOI: 10.1109/AP-S/USNC-URSI47032.2022.9886576.

[11] "5G-teknik", Accessed: Jul. 1, 2020, *Strålsäkerhetsmyndigheten*. [Online] Available: https://www.stralsakerhetsmyndigheten.se/omraden/magnetfalt-och-tradlos-teknik/5g-teknik/.

[12] G. Izydorczyk, K. Mikula, D. Skrzypczak, K. Moustakas, A. Witek-Krowiak, and K. Chojnacka, "Potential environmental pollution from copper metallurgy and methods of management", *Environmental Research*, vol. 197, p. 111 050, 2021. DOI: https://doi.org/10.1016/j.envres.2021.111050.

[13] A. Kishk, "Fundamentals of antennas", *Antennas for Base Stations in Wireless Communications*, p. 1, Jan. 2009. [Online]. Available: https://www.researchgate.net/publication/224833012.

[14] D. K. Cheng, *Field and Wave Electromagnetics*, Pearson new international editon. Pearson Eduaction, 2014.

[15] H. Kaouach. "Antenna theory: Lecture #2 antennas". (Jan. 2016), [Online]. Available: https://doi.org/10.13140/RG.2.1.4319.0802.

[16] F. Gustrau, *RF and Microwave Engineering: Fundamentals of Wireless Communications, Fundamentals of Wireless Communications* (New York Academy of Sciences Series), English, 1st ed. John Wiley & Sons, Incorporated, Aug. 2012, ch. 7, pp. 249–293.

[17] "Fundamental parameters and definitions for antennas", in *Modern Antenna Handbook*. 2008, pp. 1–56. DOI: 10.1002/9780470294154.ch1.

[18] e. Volakis John L., "Far-field antenna properties, power transfer, and reciprocity", in *Antenna Engineering Handbook*, 5th, New York: McGraw-Hill Education, 2019, ch. 1.4. [Online]. Available: https://www.accessengineeringlibrary.com/content/book/9781259644696/toc-chapter/chapter1/section/section5.

[19] N. Ida, "Antennas and electromagnetic radiation", in *Engineering Electromagnetics*, Cham: Springer, 2021, ch. 18. DOI: 10.1007/978-3-030-15557-5_18.

[20] Y. Huang, "Radiation efficiency measurements of small antennas", in *Handbook of Antenna Technologies*, Z. N. Chen, Ed. Singapore: Springer Singapore, 2014, pp. 1–21. DOI: 10.1007/978-981-4560-75-7_71-1.

[21] D. M. Pozar, *Microwave Engineering*, 4th ed. John Wiley & Sons, Inc., Hoboken, New Jersey, 2012.

[22] e. Volakis John L., "Far-field antenna properties, power transfer, and reciprocity", in *Antenna Engineering Handbook*, 5th, New York: McGraw-Hill Education, 2019, ch. 1.6.

[23] J. Huang, "Microstrip antennas: Analysis, design, and application", in *Modern Antenna Handbook*. John Wiley Sons, Ltd, 2008, ch. 4, pp. 157–200. DOI: https://doi.org/10.1002/9780470294154.ch4.

[24] J. E. Roy and L. Shafai, "Generalization of the ludwig-3 definition for linear copolarization and cross-polarization", in *1996 Symposium on Antenna Technology and Applied Electromagnetics*, 1996, pp. 645–654.

[25] A. Kumar, A. Q. Ansari, B. K. Kanaujia, J. Kishor, and L. Matekovits, "A review on different techniques of mutual coupling reduction between elements of any mimo antenna. part 1: Dgss and parasitic structures", *Radio Science*, vol. 56, no. 3, e2020RS007122, 2021. DOI: https://doi.org/10.1029/2020RS007122.

[26] e. Volakis John L., "Far-field antenna properties, power transfer, and reciprocity", in *Antenna Engineering Handbook*, 5th, New York: McGraw-Hill Education, 2019, ch. 1.9.

[27] "The Role of Massive MIMO in 5G Networks", *Ericsson*, Accessed: Feb. 16, 2022. [Online] Available: https://www.ericsson.com/en/reports-and-papers/ericsson-technology-review/articles/using-massive-mimo-to-meet-5g-network-requirements.

[28] D. M. V. S. Panchami S V, "A review on mimo systems with antenna selection", *International Journal of Engineering Research Technology (IJERT) NCICCNDA*, vol. 5, no. 22, 2017.

[29] R. J. Mailloux, *Phased Array Antenna Handbook*, 2nd ed. Norwood, MA, USA: Artech House, Inc., 2005.

[30] R. NishaBegam and R. Srithulasiraman, "The study of microstrip antenna and their applications", in *2015 Online International Conference on Green Engineering and Technologies (IC-GET)*, Nov. 2015, pp. 1–3. DOI: 10.1109/GET.2015.7453852.

[31] H. Okuno, T. Tominaka, S. Fujishima, *et al.*, "Design study of the injection and extraction systems for the riken superconducting ring cyclotron", in *1998 IEEE International Integrated Reliability Workshop Final Report (Cat. No.98TH8363)*, 1998, 1075–1077 vol.1. DOI: 10.1109/IRWS.1998.745385.

[32] D. Guha and Y. M. M. Antar, Eds., *Microstrip and Printed Antennas, New Trends, Techniques and Applications*, English, 1st ed. John Wiley & Sons, Incorporated, Dec. 2010, ch. 1, pp. 1–33.

[33] R. Akhbar, Z. Faiza, A. Mozi, F. Mohd Atan, and N. Anuar, "Aperture coupled microstrip antenna with different substrate thickness", Aug. 2013, pp. 98–102. DOI: 10.1109/ICSGRC.2013.6653283.

[34] A. Bediaf, M. Bedra, W. Allaoua, *et al.*, "Unlocking enhanced bandwidth for 5g microstrip antennas: A comparative analysis of substrate anisotropy and thickness manipulation techniques", in *2023 International Conference on Electrical Engineering and Advanced Technology (ICEEAT)*, vol. 1, 2023, pp. 1–4. DOI: 10.1109/ICEEAT60471.2023.10426321.

[35] S. S. Chakravarthy, N. Sarveshwaran, S. Sriharini, and M. Shanmugapriya, "Comparative study on different feeding techniques of rectangular patch antenna", in *2016 Thirteenth International Conference on Wireless and Optical Communications Networks (WOCN)*, 2016, pp. 1–6. DOI: 10.1109/WOCN.2016.7759032.

[36] A. Sulima, "Cavity-backed slot antenna", in *IEEE Antennas and Propagation Society International Symposium. Digest. Held in conjunction with: USNC/CNC/URSI North American Radio Sci. Meeting (Cat. No.03CH37450)*, vol. 4, 2003, 494–496 vol.4. DOI: 10.1109/APS.2003.1220318.

[37] T. Hikage, M. Omiya, and K. Itoh, "Considerations on performance evaluation of cavity-backed slot antenna using the fdtd technique", *IEEE Transactions on Antennas and Propagation*, vol. 49, no. 12, pp. 1712–1717, 2001. DOI: 10.1109/8.982450.

[38] Q. Rao, T. Denidni, and R. Johnston, "A new aperture coupled microstrip slot antenna", *Antennas and Propagation, IEEE Transactions on*, vol. 53, pp. 2818–2826, Oct. 2005. DOI: 10.1109/TAP.2005.854521.

[39] *Ansys HFSS | 3D High Frequency Simulation Software — ansys.com*, https://www.ansys.com/products/electronics/ansys-hfss, [Accessed 10-04-2024].

[40] Eurocircuits, *Tolerances on Printed Circuit Boards - Eurocircuits — eurocircuits.com*, https://www.eurocircuits.com/tolerances-on-a-pcb/, [Accessed 27-03-2024].

[41] *RO4000&xAE; Series Laminates — rogerscorp.com*, https://www.rogerscorp.com/advanced-electronics-solutions/ro4000-series-laminates, [Accessed 27-03-2024].

[42] ALL, *SMPM Male PCB Surface Mount Connector, R/A, FD — svmicrowave.com*, https://www.svmicrowave.com/smpm-male-pcb-surface-mount-connector-ra-fd, [Accessed 27-03-2024].

[43] M. H. C. Dias, B. R. Franciscatto, E. M. B. Nogueira, and T. P. Vuong, "On the Design of a Dual-Fed Aperture-Coupled Circularly Polarized Microstrip Patch Antenna", Rio de Janeiro, Brazil: IEEE, Aug. 2013. DOI: 10.1109/IMOC.2013.6646527. (visited on 02/02/2024).

A

S-parameters

This appendix presents the remaining plots of the simulated and measured S-parameters for the antenna.

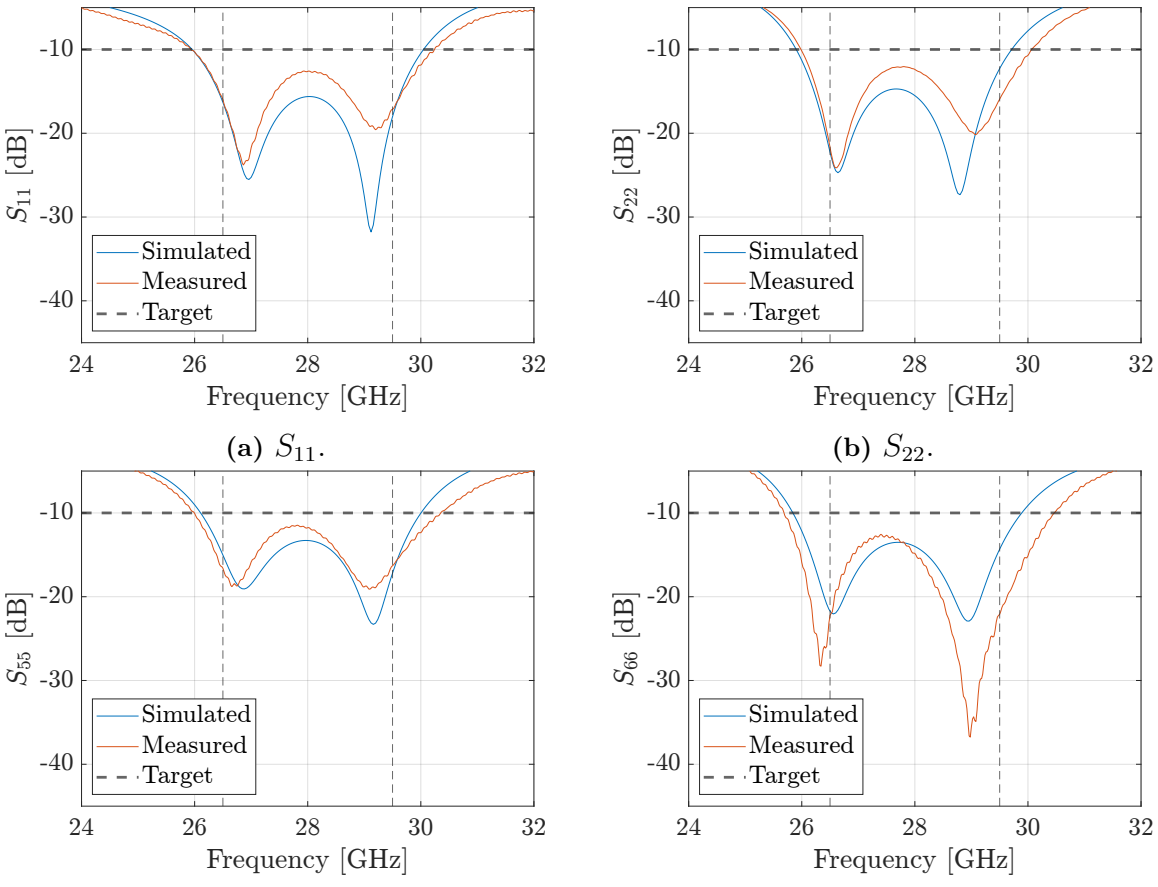

(a) S_{11}. **(b)** S_{22}.

(c) S_{55}. **(d)** S_{66}.

Figure A.1: Rectangular plots of simulated and measured input-port reflection coefficients.

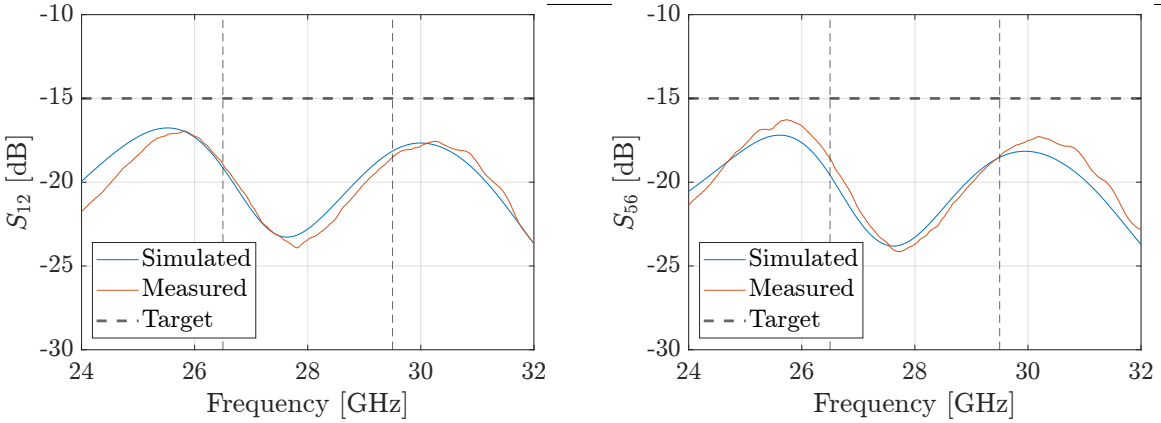

(a) S_{12}. **(b)** S_{56}.

Figure A.2: Rectangular plot of simulated and measured polarization self-coupling coefficients.

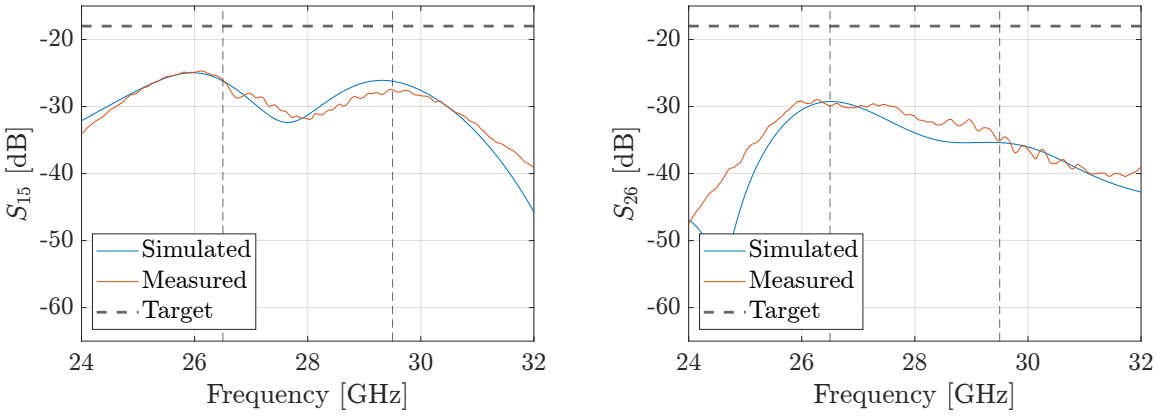

(a) S_{15}. **(b)** S_{26}.

Figure A.3: Rectangular plot of simulated and measured co-polarized element mutual coupling coefficients.

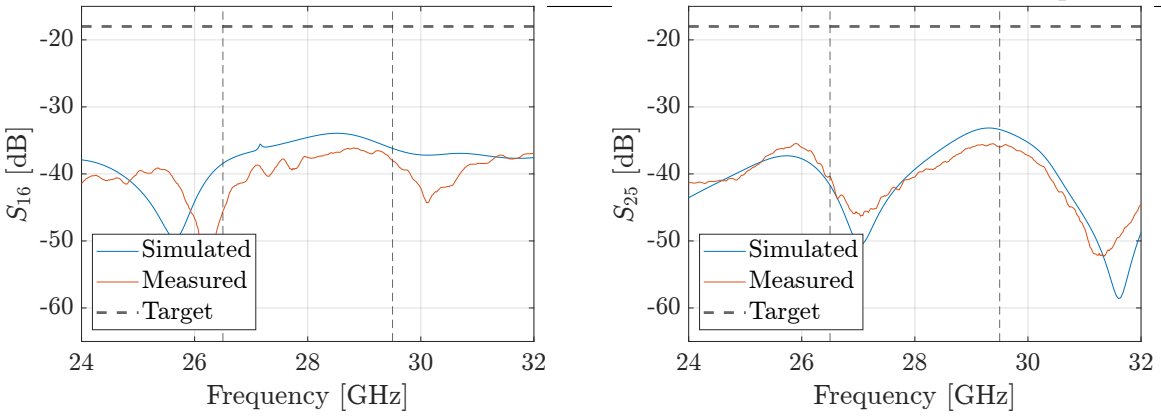

(a) S_{16}. **(b)** S_{25}.

Figure A.4: Rectangular plot of simulated and measured cross-polarized element mutual coupling coefficients.

B

Realized gain for single isolated element at other frequencies

This appendix present the results of the simulated realized gain for the single isolated element at 26.5 GHz and 29.5 GHz.

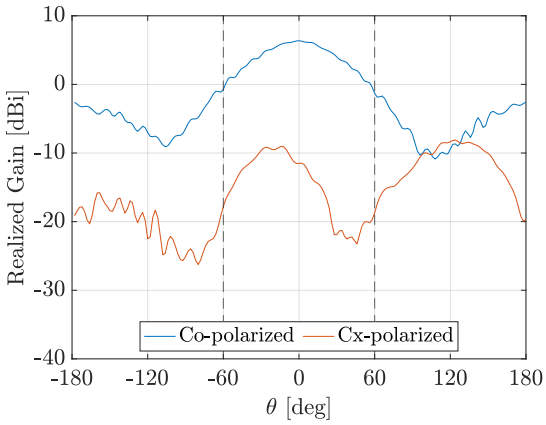

(a) $\phi = 0°$.

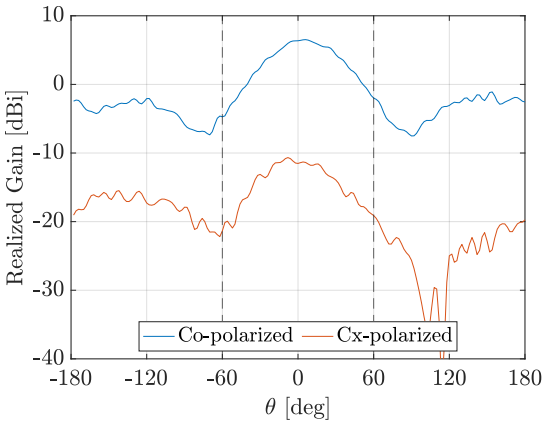

(b) $\phi = 90°$.

Figure B.1: Simulated realized gain for a H-polarized single isolated element at 26.5 GHz.

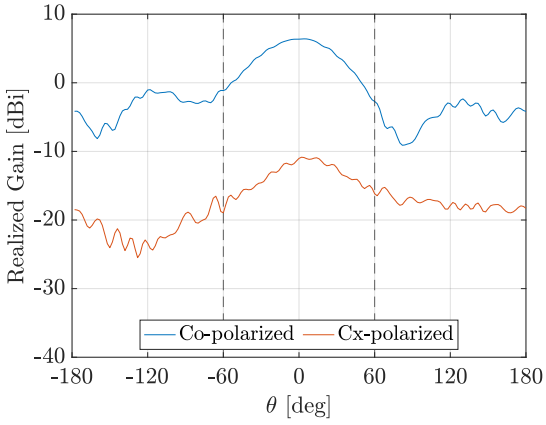

(a) $\phi = 0°$.

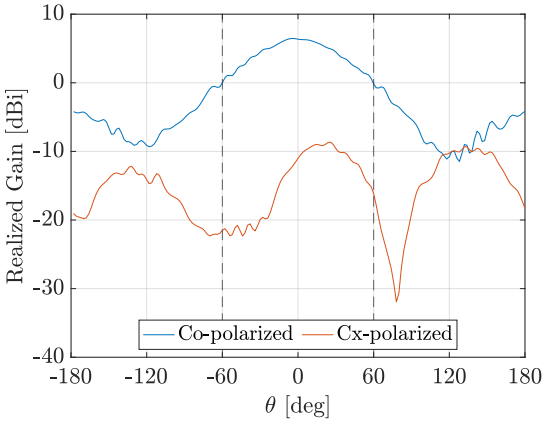

(b) $\phi = 90°$.

Figure B.2: Simulated realized gain for a V-polarized single isolated element at 26.5 GHz.

B. Realized gain for single isolated element at other frequencies

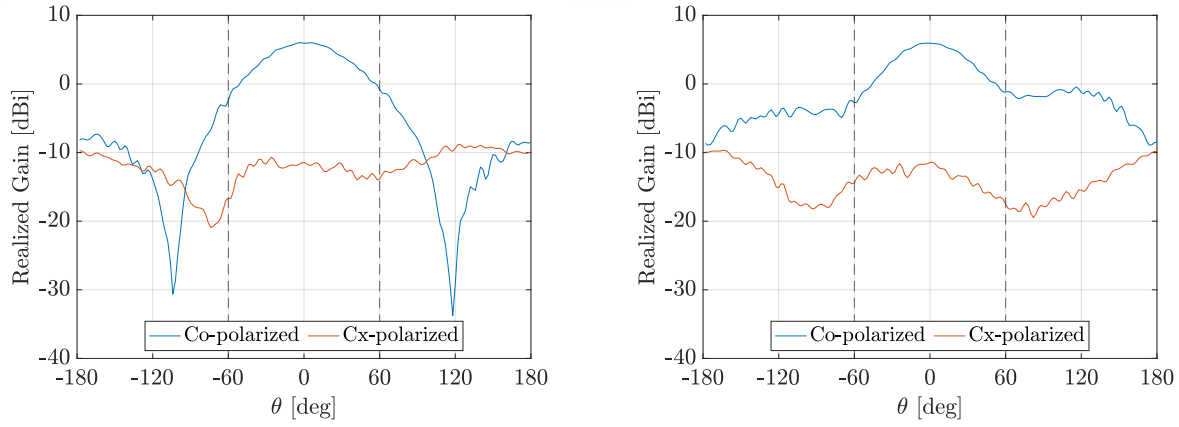

(a) $\phi = 0°$. **(b)** $\phi = 90°$.

Figure B.3: Simulated realized gain for a H-polarized single isolated element at 29.5 GHz.

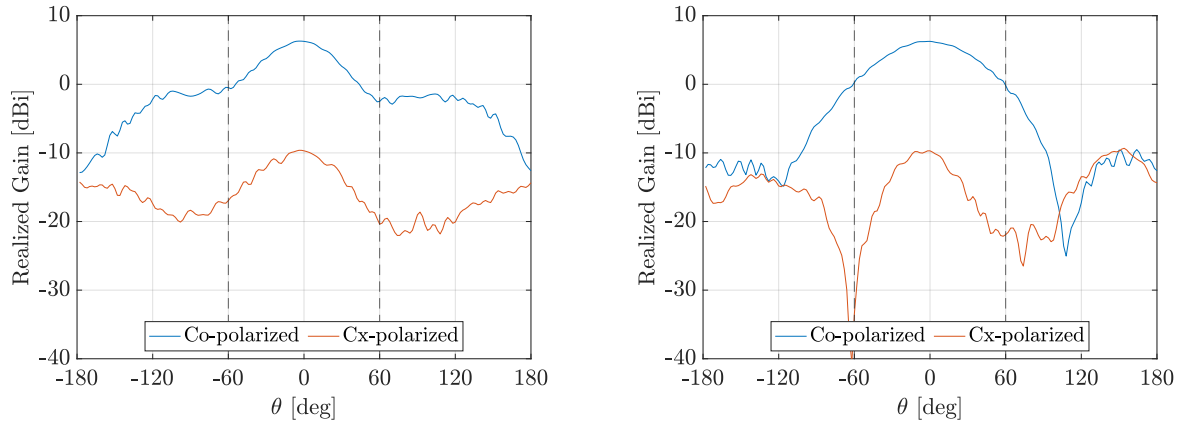

(a) $\phi = 0°$. **(b)** $\phi = 90°$.

Figure B.4: Simulated realized gain for a V-polarized single isolated element at 29.5 GHz.

C

Embedded element pattern at other frequencies

The remaining results of the simulated realized gain for the embedded element pattern at 26.5 and 29.5 GHz is presented in the appendix.

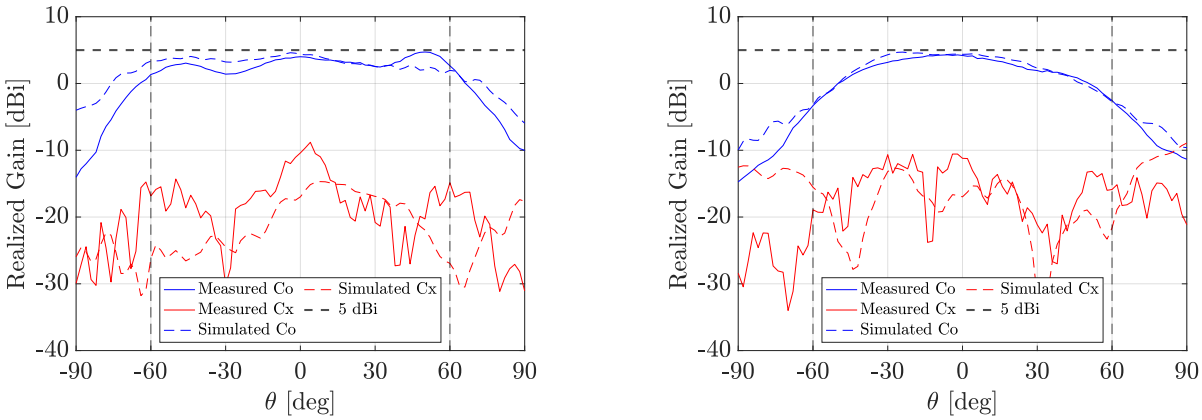

(a) $\phi = 0°$. **(b)** $\phi = 90°$.

Figure C.1: Simulated and measured realized gain for V1 for different orientations.

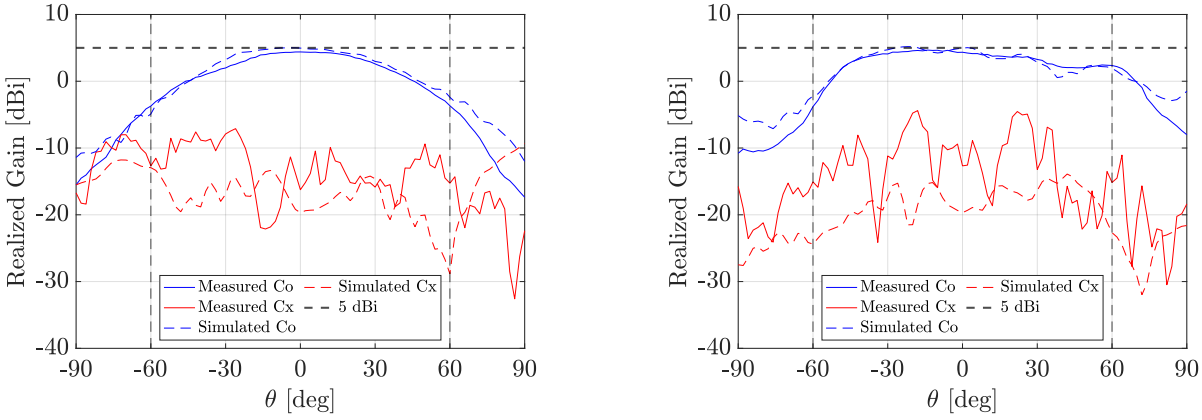

(a) $\phi = 0°$. **(b)** $\phi = 90°$.

Figure C.2: Simulated and measured realized gain for H1 for different orientations.

C. Embedded element pattern at other frequencies

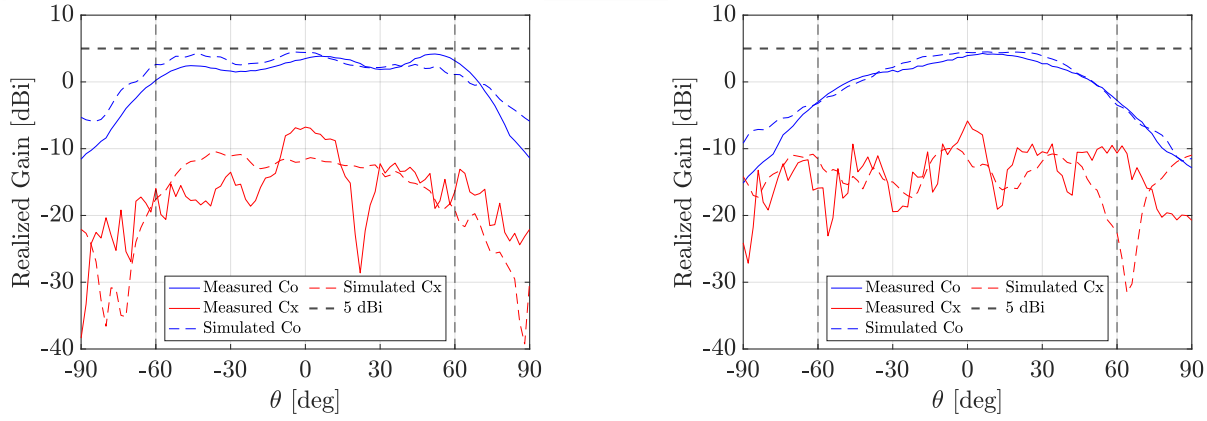

(a) $\phi = 0°$. **(b)** $\phi = 90°$.

Figure C.3: Simulated and measured realized gain for V3 for different orientations.

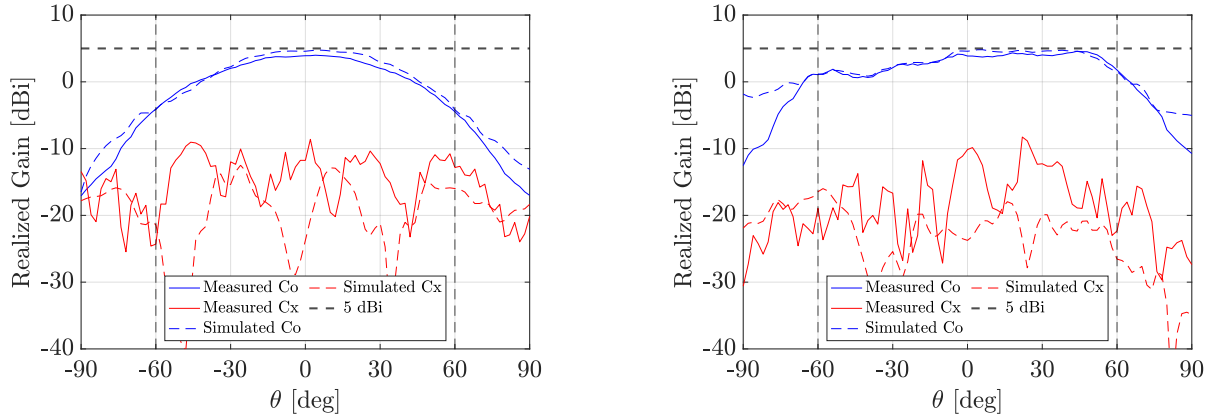

(a) $\phi = 0°$. **(b)** $\phi = 90°$.

Figure C.4: Simulated and measured realized gain for H3 for different orientations.

D

Beam steering at other frequencies

This appendix present the results of the beam steering conducted at other frequencies 26.5 GHz respective 29.5 GHz for both horizontal and vertical ports.

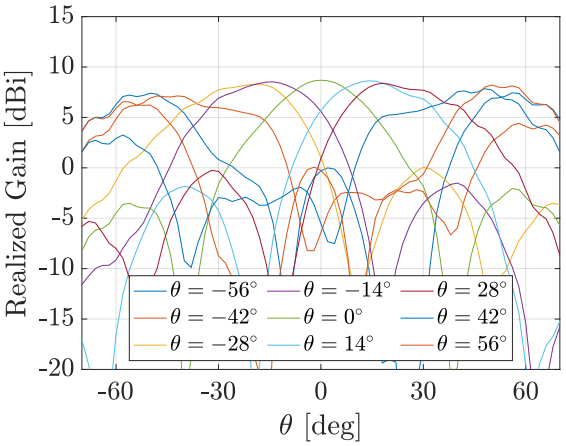

(a) H-ports at 26.5 GHz.

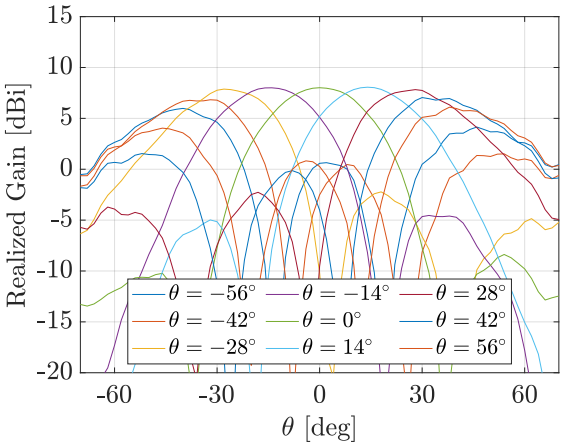

(b) H-ports at 29.5 GHz.

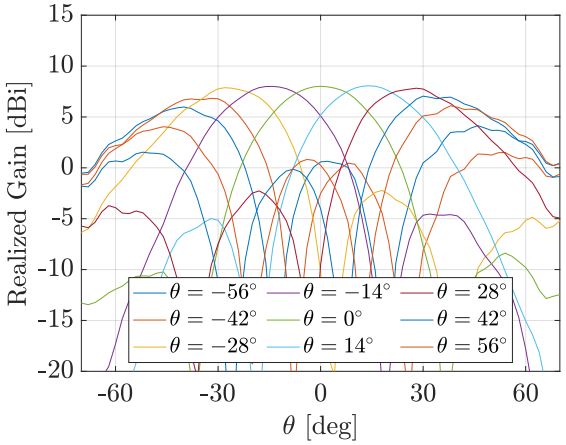

(c) V-ports at 26.5 GHz.

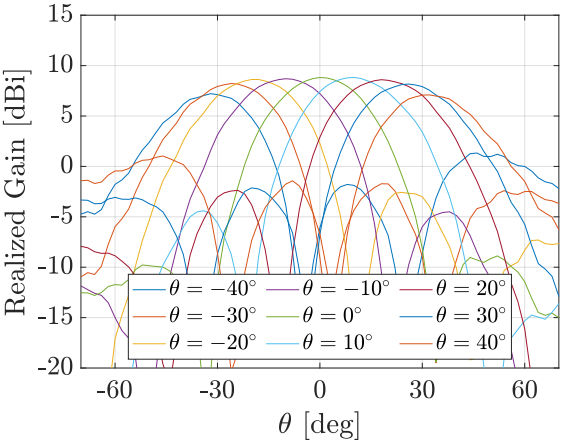

(d) V-ports at 29.5 GHz.

Figure D.1: The co-polarized realized gain from the simulated beam steering of the antenna array at two different frequencies.